Magnetohydrodynamic Levitation for High-Performance Flexible Pumps.

Yoav Matia[§1,2], Hyeon Seok An[§1], Robert F. Shepherd[†1], Nathan Lazarus[†2]
[1]Faculty of Mechanical Engineering, Cornell University Ithaca, New York 14853,
[2]ORAU Fellowship Program at Army Research Lab, 2800 Powder Mill Rd, Adelphi, MD 20783, USA
[3] U.S. Army Research Laboratory, 2800 Powder Mill Rd, Adelphi, MD, 20783, United States
[§]Equal Contributions
[†]Corresponding Authors

Abstract

We use magnetohydrodynamic levitation as a means to create a soft elastomeric solenoid-driven pump. We present a theoretical framework and fabrication of a pump designed to address the unique challenges of soft robotics, maintaining pumping performance under deformation. Using a permanent magnet as a piston, and ferrofluid as a liquid seal, we model and construct a deformable displacement pump. The magnet is driven back and forth along the length of a flexible core tube by a series of solenoids made of thin conductive wire. The magnet piston is kept concentric within the tube by Maxwell stresses within the ferrofluid, and magnetohydrodynamic levitation, as viscous lift pressure is created due to its forward velocity. The centering of the magnet reduces shear stresses during pumping and improves efficiency. We provide a predictive model and capture the transient nonlinear dynamics of the magnet during operation, leading to a parametric performance curve characterizing the elastomeric solenoid-driven pump (denoted ESP), enabling goal-driven design. In our experimental validation of this model, we report a shut-off pressure of $2-8\ [kPa]$ and run-out flow rate of $50-325\ [ml\ \mathrm{min}^{-1}]$ while subject to deformation of its own length scale, drawing a total of 0.17 watts. This performance is the highest reported work rate for a pump that operates under its own length scale deformation. We then integrate the pump into an elastomeric chassis and squeeze it through a tortuous pathway while providing continuous fluid pressure and flow rate; the vehicle then emerges at the other end and propels itself swimming.

Keywords: Magnetohydrodynamic levitation, lubrication, analytical, hydrodynamics, viscous flow, fluid-structure interaction, soft robotics, soft displacement pump.

1. Introduction

A large number of soft robots use fluidic elastomer actuators (FEAs) powered by pumps, e.g. [1–17]. These pumps, the *hearts* of soft robots, are typically electrically powered displacement pumps due to their availability, efficiency, performance curves, and control simplicity. An example of a typical electrically powered displacement pump is the BTC IIS (Parker-Hannifin) which is rigid and bulky. When used, these types of pumps necessitate centralizing them, routing the pressurized fluid via long channel lengths to the actuator locations, and use valving to control when they are pressurized, as evident in characteristic works such as Tolley et al. [18] and Aubin et al. [19].

The use of pumps with mechanical properties more similar to FEAs would allow for the decentralization and distribution of displacement pumps across the volume of soft robots. The benefits of this approach would be numerous: (i) the number of pumps in one machine could be increased for faster and more forceful robots; (ii) they could be placed in closer proximity to actuators for improved efficiency; (iii) the number of valves could potentially be reduced for smaller form factors; (iv) most importantly, the beneficial compliance of soft robots would be maintained.

In this regard, there are several promising and elegant examples of pumps made entirely of compliant materials for use in soft robots, such as that of Cacciucolo et al. [20], Diteesawat et al. [21]. Other examples [13,22–29] offer the potential for efficient, distributed fluidic actuation or analogous approaches to soft displacement and rotary pumps [30–44] and, while they all incorporate soft materials or could be envisioned as a viable pumping solution for soft robotic application; none report performance under deformation, limiting their practical application. Thus, there still remains an important need for a compliant displacement pump that offers high flow rates, $q = O(10^2)[ml\ min^{-1}]$, and pressures, $p = O(10^5)[Pa]$, at a system work point (i.e. system and pump curve intersection) compatible with human scale FEA systems, $O(10^{-1} - 10^0)[m]$. Further, scalable and continuous performance under quasi-static or dynamic deformation should also be a feature of this pump to facilitate technology transfer.

The major challenge facing the development of a deformable displacement pump is the need to maintain a seal under deformation. This means maintaining a separation between the high and low potential fluid while providing a physical gap, on the order of the local curvature, between adjacent interacting components (e.g., an impeller or piston, or equivalent within the housing, to avoid mechanical jamming). In our work, we use ferrofluids to manage this gap. Therefore, of special relevance to this work is research regarding ferrofluids' use as the medium in making a fluidic seal in either journal bearings [45–49] and other rigid applications, for example, [50–55], to name just a few. In addition, examination of rigid ferrofluid-based pumps, such as [56–61], exemplifies the inherent limitations in extending the notion of a fluidic seal to the displacing component being made entirely of liquid, i.e., making a liquid piston or vane; whereby relying on cohesion forces (i.e., surface tension) to generate appreciable pressure gradients $\Delta p = O(10^0)[kPa]$, and as these are inversely related to gap width, we have to operate in gap regimes that are too narrow for utility, resulting in very low flow rates less than $q = O(10^{-1})[ml\ min^{-1}]$.

This paper explores a novel approach to making soft robotic hearts, whereby the traditional concept of ferrofluid gap management is extended to loosely fitted magnetic cores that act as pistons and are centered by leveraging magnetohydrodynamic lubrication. The ferrofluid coating centers the core as it moves along the flexible tube and forms a seal, bridging over a specified physical gap of $C = 0.25[mm]$, selected as such to allow the magnetic core in our system to travel without jamming as the pump takes on a radius of curvature of its own length scale, $R_c \leq 100[mm]$. Further, we provide the scaling laws for magnetohydrodynamic lubrication mechanism in such systems with respect to pressure, flow rate, size, and radius of curvature, thus proposing a scalable principle mechanism for future advances in soft-pump technology.

While the field of hydrodynamic lubrication has been studied extensively over the years, with or without magnetic forces involvement, the nonlinear nature of the physics governing such systems caused prior efforts to avoid explicit dynamic solutions of the lubrication layer thickness evolution over time. Therefore, these efforts usually set the lubrication layer as constant [62,63], or consider time not as an independent variable but rather as an input parameter, setting eccentricity and rate of change as

constant [64,65]; resulting in a static problem governed by an elliptical equation. Others use planar configurations [63,66], focus on experimental and numerical examination [63,66,67], or a combination of the above.

In this paper, we present an approximate explicit solution of the predictive model for our soft robotic heart that uses perturbation theory to capture the nonlinear dynamics of magnetohydrodynamic lubrication in a non-planar configuration. We then experimentally demonstrate that this elastomeric solenoid-driven pump (ESP) can maintain continuous performance under large deformation, i.e., up to 30% in axial strain and a radius of curvature of its own length scale; as well as supply the design rules to correlate physical parameters to the desired deformation.

In Fig. 1, we provide a visualization of novelty; we show the proposed ESP operating at the largest work point yet reported for pumps that continue to operate while deformed (for literature comparison details, see SI appendix A.1). Last, we provide the insight and scaling laws required to produce a goal-driven design of this novel pump system, tailored to soft robotics unique challenges.

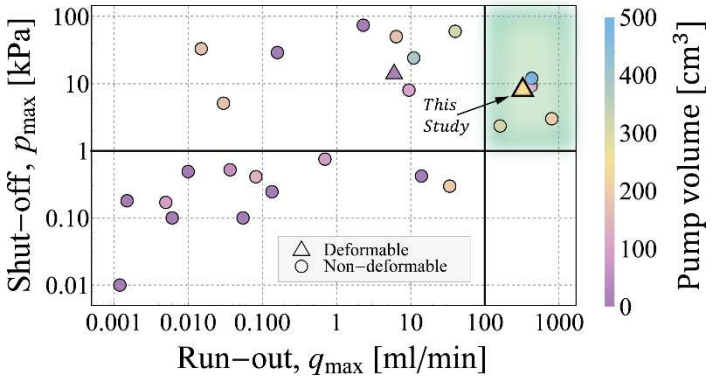

Fig. 1. ***Shut-off (max pressure no flow) Vs. Run-out (max flow now back-pressure) performance of comparable state-of-the-art systems.*** *Visualization of novelty, largest work-point reported to date for pumps that operate under large deformations (of its own length scale). All other pump technologies in its performance order-of-magnitude are non-deformable pumps.*

2. Experimental Design

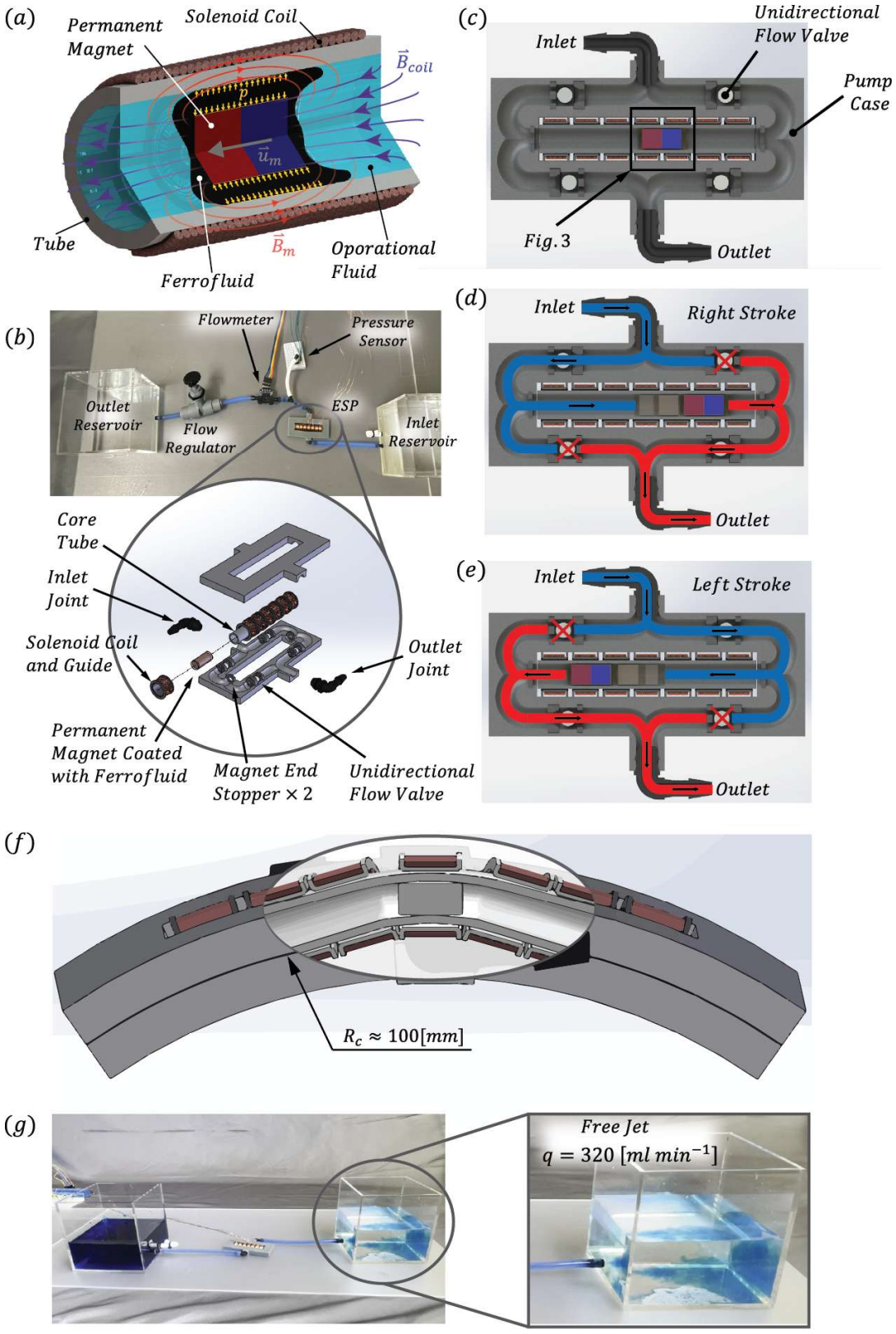

Fig. 2. ***Illustration of the elastomeric solenoid-driven pump (ESP) configuration used in both modeling and experiments.*** *(a) A three-dimensional model with key components and physical quantities. (b) Workbench setup used in the acquisition of experimental data, Inset illustrates an exploded view of the internal structure of an ESP with key top-level components. (c) Cross-section view of ESP; black frame indicates the focus of next figure, Fig. 3. (d) & (e) Cross-section view of ESP in operation. Snapshots of magnetic core right and left heading strokes with an indication for the state of the one-directional valves; red and blue fluid lines indicate high and low pressure, respectively. (f) Illustrative image of our designed ESP under deformation (bending) showing the loosely fitted magnetic core jamming upon exceeding the design-intended limit for the radius of curvature* $R_c \approx 100[mm]$*; thus emphasizing the particular importance of a goal-driven design for rigid components in our system. (g) Visualization of pump potency, generating a free jet, with flow rate measured at* $q = 320\ [ml\ min^{-1}]$.

Figure 2 presents the studied configuration of an elastically compliant soft robot heart, the ESP. In fig. 2a, we show a three-dimensional section cut and present our system's fundamental physical quantities at work. By applying current to the solenoid coil, we generate a magnetic field $\vec{B}_{coil}$, attracting a rigid permanent magnetic core of field $\vec{B}_m$, and driving it at velocity $\vec{u}_m$ via the dipole-dipole interaction. This core (interchangeably denoted the *magnetic piston core*) is sheathed with a layer of ferrofluid (FerroTec EFH1), in which hydrodynamic lubrication generates viscous pressure p by the forward motion, centering the core and preventing contact with the walls, addressed in detail in analysis section 4.1.

Fig. 2b presents the experimental workbench setup used to measure the pump performance curve outside a robotic system. We show the ESP connected to fluid reservoirs: one at the inlet and one at the outlet. The outlet tubing is fitted with a flowmeter (Renesas, FS2012-1020-NG), pressure sensor (Honeywell, SSCDANN030PAAA5), and a Precision Flow-Adjustment Valve (McMaster-Carr) providing back-pressure load. Workbench peripheral components standing in for the robotic system include: MCU (Arduino Uno) and Keithley 2400 DC power supply, providing the required 0.17[W] (1[V] and 0.17[A]). Pump assembly dimensions are $(\text{width} \times \text{length} \times \text{height}) = (40 \times 71 \times 8)\ [mm]$ and is made of silicone urethane elastomer CARBON, INC. SIL 30 with an elastic modulus of $E = 1.8[MPa]$. Inset illustrates the pump's internal structure, featuring seven solenoids of wire density $N[winding\ m^{-1}] = 5760$ threaded over the core tube, magnet end stoppers, inlet and outlet joints, and four unidirectional flow valves. For more details, see SI appendix section A.2.

In Fig. 2c-2e, we illustrate the role of the four integrated flow valves, creating unidirectional flow from inlet to outlet as the magnetic core piston is cycled back and forth along the core tube. Red cross-marks denote which valves are at closed state, and red and blue fluid lines indicate high and low pressure, respectively.

Particular attention is given to the dimensioning of rigid components within our system, i.e., ball bearings, solenoid coils, and the magnetic piston core. The ball bearings (used for the unidirectional valves) add no constraint on the system's elastic compliance, being in a loose fit of their own length scale ($d_{ball} \approx 3.5[mm]$). Conversely, the pump's ability to maintain continuous performance under elastic deformation is restricted by the solid magnet piston core and the number of solenoids, limiting bending deformation as would a vertebra. First, we set the pump's operational envelope and require continuous operation under deformation of its own length scale; we thus set the limit for the radius of curvature to be $R_c \approx 100[mm]$, see illustrated in Fig. 2f. We then select the magnetic piston core to match the overall scale of the pump assembly, namely a commercially available N52 Neodymium magnet with a diameter of $d_m = 2r_m = 4[mm]$ and a length $l = 6.315[mm]$; in accordance with which we determine the length of the solenoid coils $l_c = l$. Having established the piston core dimensions and curvature limits, we can then determine the gap required, $C = 0.25[mm]$, and respectively the diameter of the enveloping tube inner wall $d_w = 2r_w = 4.5[mm]$. For a detailed discussion on bending strain relation to geometric parameters, see Results section, see SI appendix section A.3.

3. Experiment Procedure

Using our benchmark setup, see Fig. 2b, we characterize pump performance at both deformed and free state. We start the system from rest with the flow regulator fully closed and initiate the MCU supplying $1[V]$ and $0.17[A]$ to the solenoid train. We then set the nominal solenoid relay period to $\tau_r \approx 0.019[sec]$, i.e., the activation period of a solenoid in a sequence. Based on the viscous-elastic characteristic time scale $t^* \sim \pi l \mu / \epsilon^2 \kappa_f$ (see derivation at analysis section 4.1) we calculate the system achieving steady-state after a time scale of the order $t^* \approx 0.113[sec]$. To assure we have achieved steady-state prior to collecting data, we allow the system one minutes to stabilize. We then take pressure

sensor readings and evaluate flow rate using both a flowmeter and by collecting the outlet spillage for two minutes in a $1000[ml]$ glass beaker, and normalize for water density at room temperature. Repeating this process for twenty measuring points, differentiated by incrementally increasing flow rate using the flow regulator, we generate the pump performance curve. Experimental data for all plots in this work represents one-sigma certainty acquired over seven experiments per pump, and five separate pumps tested.

Fig. 2g offers a visual indication of the pump's potency, generating a free jet with a flow rate measured at $q = 320\ [ml\ min^{-1}]$. We report continuous performance in the order of $p = O(1)[kPa]$ and $q = O(10^2)[ml\ min^{-1}]$ over a range of elastic deformation up to a radius of curvature of the pump's length scale. For a detailed discussion of scaling laws for geometry, deformation, and performance, please refer to the Analysis and Results sections.

4. Analysis

Providing the theoretical framework for our experimental system, we present two separate models for two separate governing mechanisms in the system. Together these provide insight and predict the system's dynamic behavior. The first is the single-phase lubrication layer: we calculate the friction and pressure inside the fluid seal domain using lubrication theory. Integrating with the force balance equations, we correlate back-pressure Δp, downstream effective flow velocity u_m and electromagnetic actuating force $\boldsymbol{f}_b$, see equation (1.11). The model assumes $u_m = u_{mag}$, where u_{mag} is the effective average velocity of the magnet during operation. Furthermore, it is assumed that the product of u_m and core tube-inner cross section gives us the pumped flow rate $q[ml/min]$ vs pressure $\Delta p[Kpa]$; predicting the nonlinear inverse relation of the pump's performance curve.

The second provides the mechanism correlating the abovementioned prediction with our experiments, where the actual magnet velocity $u_{mag} = z_0/\tau_r$ is held constant fixing the solenoid relay time actuation τ_r. We are then left to reason the means by which a constant velocity-driven positive displacement pump provides a varying flow rate. We utilize the equation-based modeling capabilities of COMSOL Multiphysics 5.5 (see SI appendix section 0), and show the emergence of Taylor-Saffman instability, i.e., viscous fingers, with a unique stable developed pattern emerging in the presence of the

system's restoring magnetic force. We thus show how an effective flow rate "leak" dependent on back-pressure Δp is maintained past the liquid seal to enforce mass conservation.

4.1. Lubrication Theory Modeling, Prediction of the Nonlinear Inverse Relation of Pressure to Flow Rate.

We begin by formulating the predictive model characterizing the steady-state and dynamic performance of an ESP. It consists of a cylindrical core tube inside which a levitated magnetic core coated with ferrofluid. This coating provides a seal capable of maintaining its integrity as the pump deforms during operation and the viscous pressures required for magnetohydrodynamic levitation to prevent the solid-fluid piston from jamming during operation. Fig. 3a illustrates the axial cross-section of the proposed system. Fig. 3b, 3c illustrates the magnet axial degrees of freedom; solenoid wire is omitted for visual clarity.

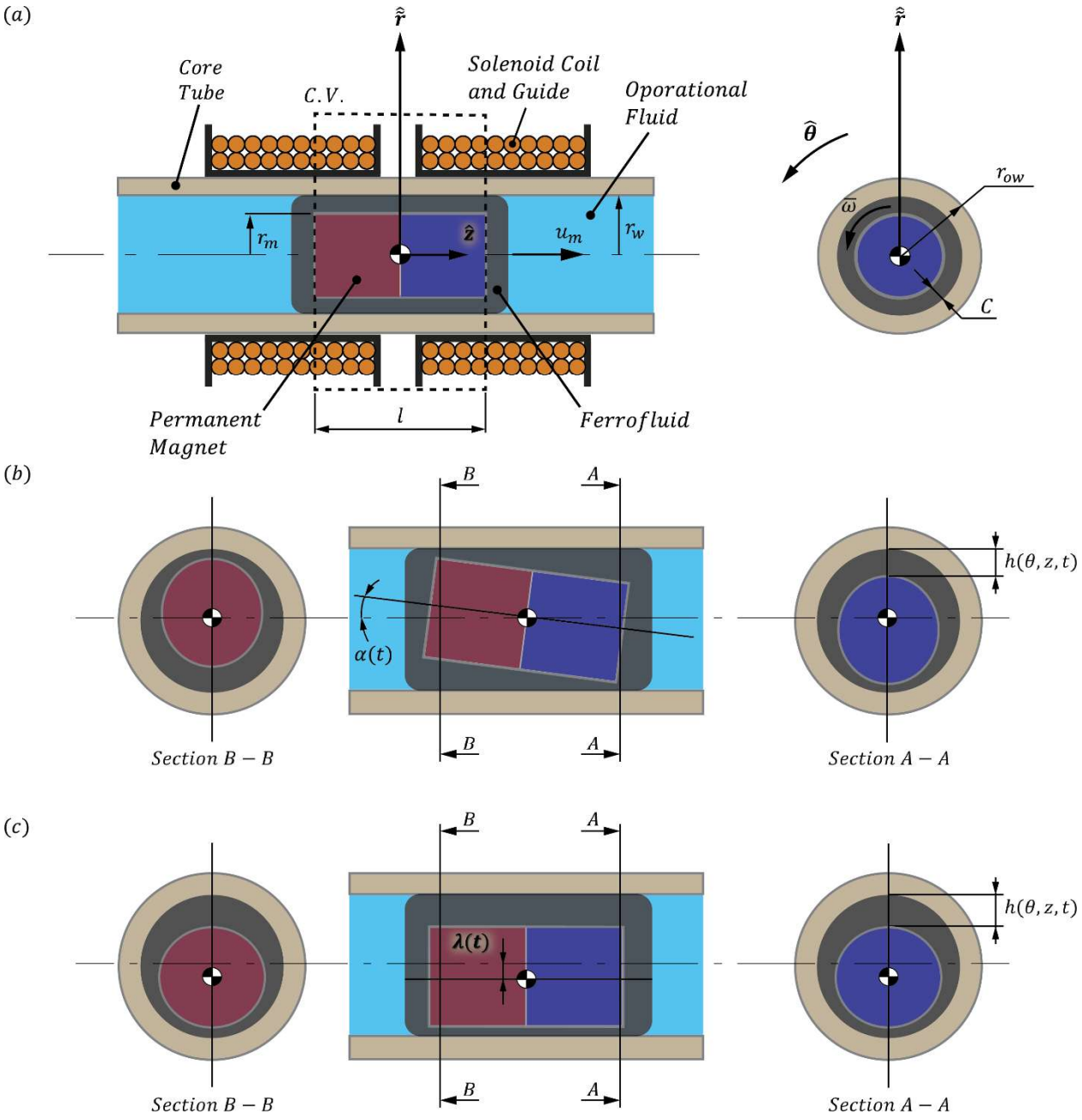

Fig. 3. ***System Geometry including section views for visual clarity.*** *(a) System axial cross-section with the magnetic core axially centered. (b) Illustrating angular deviation of the magnetic core from a coaxial position. (c) Illustration of respective parallel deviation. For plates (b) and (c), the solenoid coil surrounding the core tube was omitted for visual clarity.*

In order to gain insight into the performance of an ESP system and the results presented here, we aim to model both the magnet dynamics during a stroke in the reciprocating cycle (Fig. 4a, 4b) and the performance curve describing the pump performance fully (Fig. 4c). Based on the effective downstream fluid velocity u_m set to be the average magnet forward velocity u_{mag}, and knowing core

tube-inner cross-section, we can calculate the pumped flow rate $q[ml\,min^{-1}]$ versus pressure $\Delta p[kPa]$.

We define vector variables using bold letters, direction vectors by hat notation, non-dimensional variables by capital letters, characteristic values by an asterisk, and respective nth order-of-magnitude by a superscript (n). We define the small parameter $\epsilon = C/l$, where C and l are magnet-wall gap at the concentric position, and the magnet length, respectively. We limit axial eccentricity by the ferrofluid gap $\lambda(t) \leq C$, as well as angular misalignment $(\alpha(t)l)/2 \leq C$; we set tube radial and axial deformation due to fluid pressure to be negligible, and finally, both tube and magnetic core do not rotate about their axis. We consider the one-phase flow of ferrofluid seal in the narrow gap between the magnetic piston and the bounding tube wall as the magnet is driven forward. We assume the ferrofluid to be Newtonian and incompressible, and by way of lubrication approximation [65], we formulate our governing equations for mass $\nabla \cdot \boldsymbol{u} = 0$, and momentum conservation, in terms of the Stokes equation $\nabla p = \mu \nabla^2 \boldsymbol{u}$. We define a moving, gap curvilinear cylindrical frame $(\hat{\boldsymbol{r}}, \hat{\boldsymbol{\theta}}, \hat{\boldsymbol{z}})$ centered at the magnet center of mass; where we define the curvilinear gap coordinate $\tilde{r}$ to range from $\tilde{r} = 0$ at the magnetic core surface (respective to cylindrical r_m in fig. 3a) to $\tilde{r} = h$ at the enveloping tube inner wall (respective cylindrical r_w in fig. 3a). We then set our system's boundary and initial conditions: the magnetic core translates axially $u_r(\tilde{r} = 0, \theta, z, t) = -\frac{\partial h}{\partial t}$, but does not rotate $u_\theta(\tilde{r} = 0, \theta, z, t) = \bar{\omega} = 0$, as the magnet is driven forward at $u_z(\tilde{r} = 0, \theta, z, t) = u_m$; the enveloping tube (i.e. core tube) is at rest $u_r(\tilde{r} = h, \theta, z, t) = 0$, $u_\theta(\tilde{r} = h, \theta, z, t) = 0$, $u_z(\tilde{r} = h, \theta, z, t) = 0$, and the entire system starts from rest $u_r(\tilde{r}, \theta, z, t = 0) = 0$, $u_\theta(\tilde{r}, \theta, z, t = 0) = 0$, $u_z(\tilde{r}, \theta, z, t = 0) = 0$. Last, we limit for small tilt angles $\alpha(t) \ll 1$ as $C \ll l$, and solve to obtain in dimensional form a special case of the Reynolds equation,

$$-\frac{\partial h^{(0)}}{\partial t} = -\frac{1}{12\mu}\frac{\partial}{\partial z}\left(\frac{\partial p^{(0)}}{\partial z}\left(h^{(0)}\right)^3\right) + \frac{u_m}{2}\frac{\partial h^{(0)}}{\partial z}; \tag{1.1}$$

relating the ferrofluid viscous pressure field $p^{(0)}(\theta, z, t)$ with magnet radial position via gap height $h^{(0)}(\theta, z, t)$. Solving for viscous pressure $p^{(0)}$ with $p^{(0)}(\theta, z = l/2, t) = \Delta p_{pump}$ and $p^{(0)}(\theta, z =$

$-l/2,t)=0$, we then provide an explicit form for pressure and axial velocity profiles as dependent on the movement of the magnet inside the encapsulating core tube,

$$p^{(0)}(\theta,z,t)=\frac{12\cos\theta}{(1+\lambda(t)\cos\theta)^3}\frac{\partial\lambda(t)}{\partial t}\frac{\mu}{\epsilon^2}\left(\frac{z^2}{2l^2}-\frac{1}{8}\right)+\Delta p_{pump}\left(\frac{z}{l}+\frac{1}{2}\right), \tag{1.2}$$

$$u_z^{(0)}(\tilde{r},\theta,z,t)=\frac{1}{2}\left(\frac{12\cos\theta}{(1+\lambda(t)\cos\theta)^3}\frac{\partial\lambda(t)}{\partial t}z+\frac{l\epsilon^2}{\mu}\Delta p_{pump}\right)\left(\frac{\tilde{r}^2-h\tilde{r}}{l^2\epsilon^2}\right) - u_m\left(\frac{\tilde{r}}{h}-1\right), \tag{1.3}$$

and the characteristic scale for pressure $p^*\sim\mu u_m/l\epsilon^2$ and kinematics of the ferrofluid field $\epsilon\sim C/l\sim C/r_m\sim u_r^*/u_m$. The observed pressure scaling implies very large pressures of the order $O(1/\epsilon^2)$ generated by any deviation from the concentric position of the magnet λ, and its temporal transients $\partial\lambda/\partial T_v$; Dominating the restoring mechanism and balancing the destabilizing back-pressure Δp acting to bring the magnet in contact with the wall, stalling the pump under coulombic friction. For more details, see SI appendix section A.4.

Next, we address the force balance equations governing our system's nonlinear dynamics in leading order. The magnet force balance equations detail the dynamic balance of Maxwell stress terms, as are the result of dipole-dipole interaction between magnet and solenoid, with those from viscosity, gravity, and the rheology, with the latter resulting from the ferrofluid held by the magnetic field of the permanent magnet,

$$\hat{\boldsymbol{z}}:\ \underbrace{f_{b,2\to1,z}^{(0)}}_{\substack{Magnetic\ dipole\\ Maxwell\ force}}+\underbrace{\int_0^{2\pi}\int_{-l/2}^{l/2}\mu\left(\frac{\partial u_z^{(0)}}{\partial\tilde{r}}\right)\Big|_{\tilde{r}=0}dz\,l\epsilon d\theta}_{Circumferential\ friction\ pressure\ drop}-\underbrace{ma_z}_{\substack{External\ system\\ acceleration\\ force,\ z-axis}}-\underbrace{\pi(l\epsilon)^2\Delta p}_{\substack{Pressure\ drop\\ across\ piston}}=0, \tag{1.4}$$

$$\hat{\tilde{\boldsymbol{r}}}:\ \underbrace{f_{b,2\to1,\tilde{r}}^{(0)}}_{\substack{Magnetic\ dipole\\ Maxwell\ force}}+\underbrace{\left(\int_0^{2\pi}\int_{-l/2}^{l/2}-p^{(0)}\cos(\theta)\,dz\,l\epsilon d\theta\right)\cos(\beta)}_{\substack{Axial\ viscous\ pressure\ lift\\ force}}+\underbrace{\kappa_f l\epsilon\lambda(t)}_{\substack{Ferrofluid\\ elastic\\ force}}-\underbrace{ma_{\tilde{r}}}_{\substack{External\ system\\ acceleration\\ force,\tilde{r}-axis}} + \underbrace{\gamma\mu u_m C}_{\substack{Center-of\\ -pressure\\ force}}=0\,. \tag{1.5}$$

Where μ and κ_f are the ferrofluid's effective dynamic viscosity and linear spring coefficient, and γ is the center-of-pressure coefficient that relates the forward velocity to the destabilizing normal force in the $\tilde{r}$ direction exerted on the levitated magnetic piston, which acts as an inverted pendulum.

For simplicity, we formulate $\boldsymbol{f}_{b,2\to1}$, the force applied by the solenoid (marked by index 2) on the permanent magnet (marked by index 1), using Ampere's model [68–75] to formulate the magnet-solenoid interaction. We assume the leading-order contribution is attributed to a point-like dipole-dipole interaction, with negligible correction resulting from mutual induction and magnet geometry (see SI appendix section A.4.2). We then formulate the magnetic dipole maxwell force,

$$\underbrace{\boldsymbol{f}_{b,2\to1}}_{\substack{Force\ by\ the\ magnetic\\ field\ of\ \ 2\ \ acting\ on\ 1}} = \underbrace{-\frac{3\mu_0\mu_r m_{1,z} N l_c I \pi r_{ow}^2}{4\pi\left(\sqrt{C^2\lambda^2+\tilde{z}(t)^2}\right)^4}}_{Force\ scalar\ magnitude}\left(\underbrace{\frac{C^3\lambda^3-4C\lambda\,\tilde{z}(t)^2}{\left(\sqrt{C^2\lambda^2+\tilde{z}(t)^2}\right)^3}}_{\hat{r}},\underbrace{0}_{\hat{\theta}},\underbrace{\frac{3\,\tilde{z}(t)C^2\lambda^2-2\tilde{z}(t)^3}{\left(\sqrt{C^2\lambda^2+\tilde{z}(t)^2}\right)^3}}_{\hat{z}}\right), \tag{1.6}$$

where $\mu_0 = 4\pi\cdot10^{-7}[N\,A^{-2}]$ is the permeability of free space, $\mu_r[1]$ the relative permeability of the ferrofluid, $m_{1,z}[A\,m^2]$ the permanent magnet magnetic moment, $N[winding\ m^{-1}]$ wire coiling density or the number of windings per unit length assuming all are a single layer winding, $I[A]$ the current running through the coil, and $l_c[m]$ the length of a single solenoid coil.

Under the above assumptions, of downstream fluid velocity u_m equals averaged magnet forward velocity u_{mag}; actuation periodicity can be related to dipole-dipole actuation distance as a function of time by the sawtooth wave function,

$$\tilde{z}(t) = u_m\tau_r\left(1-\frac{A}{2}+\frac{A}{\pi}Arctan\left(Cot\left(\frac{\pi\,t}{\tau_r}\right)\right)\right); \tag{1.7}$$

where τ_r is the solenoid relay period time, that is the period for the successive coil actuation, and $A[1]$ the temporal coordinate strain coefficient constraining an upper limit for the magnetic force during actuation in the proposed simplified model (see SI appendix section A.4.2). Substituting (1.2), (1.3), (1.6), (1.7) into our force balance equations (1.4), (1.5); setting $\Delta p_{pump} = \Delta p$, thus require force equilibrium between pump and external load; last, applying scaling arguments for magnet length $Z = z/l$, gap coordinate $R = \tilde{r}/C$, time normalized by effective downstream fluid velocity $T_v = u_m t/l$, gap height $H = h/C$, fluid field pressure $P = p/p^*$, and velocities $U_z = u_z/u_m$, $U_\theta = u_\theta/u_r^*$ and $U_r = u_r/u_r^*$, with the measure of eccentricity λ intrinsically non-dimensional thus remains unchanged. We

obtain a non-dimensional leading order force balance in the $\tilde{r}$-axis detailing the transient of magnet position during pumping operation,

$$\underbrace{\left(\frac{t^*}{t_v^*}\right)\frac{\left(2\lambda^2(T_v)+1\right)}{\left(1-\lambda^2(T_v)\right)^{5/2}}\frac{\partial\lambda(T_v)}{\partial T_v}}_{\substack{Axial\ viscous\ pressure\ lift\\ force\ term}}+\underbrace{\lambda(T_v)}_{\substack{Ferrofluid\\ elastic\\ force\ term}}-\underbrace{\varrho}_{\substack{System\\ acceleration\\ force\ term}}+\underbrace{\psi}_{\substack{Center-of\\ -pressure\\ force\ term}}=0\,, \tag{1.8}$$

With resulting characteristic scales for viscous-elastic time scale $t^*\sim\pi l\mu/\epsilon^2\kappa_f$ the kinematic time scale $t_v^*\sim l/u_m$, and two non-dimensional numbers $\varrho=(radial\ accleration)/(Elastic\ forces)=ma_{\tilde{r}}/\kappa_f C$ and $\psi=(Destabilizing\ pressure)/(Elastic\ forces)=\gamma\mu u_m/\kappa_f$. Using singular asymptotic expansion, we obtain an approximate explicit solution in leading-order (see SI appendix section A.4.3),

$$\lambda(T_v)\approx\frac{(\rho-\psi)\left(\mathrm{e}^{\rho T_v\left(\frac{t_v^*}{t^*}\right)+T_v\left(\frac{t_v^*}{t^*}\right)}-\mathrm{e}^{T_v\psi\left(\frac{t_v^*}{t^*}\right)}\right)}{\rho\mathrm{e}^{T_v\psi\left(\frac{t_v^*}{t^*}\right)}+\mathrm{e}^{\rho T_v\left(\frac{t_v^*}{t^*}\right)+T_v\left(\frac{t_v^*}{t^*}\right)}-\psi\mathrm{e}^{T_v\psi\left(\frac{t_v^*}{t^*}\right)}}. \tag{1.9}$$

Good agreement is evident in predicting the magnet position's time evolution between the numerical solution of (1.8) and the leading order explicit approximation (1.9), see Fig. 4a.

The z-axis provides us with the pressure to flow rate relation and subsequent performance curve for elastomeric solenoid-driven pumps,

$$\underbrace{\beta\frac{1}{\tilde{Z}^4(T_v)}}_{\substack{Magnetic\ dipole\\ Maxwell\ force\\ term}}\underbrace{-\frac{2}{\sqrt{1-\lambda^2(T_v)}}}_{\substack{Viscous\ friction\\ pressure\ drop\\ term}}-\underbrace{\zeta}_{\substack{System\\ acceleration\\ force\ term}}-\underbrace{2\,\Delta P}_{\substack{Pressure\ drop\\ across\ piston\\ term}}=0\,; \tag{1.10}$$

along with respective non-dimensional numbers $\beta=(maxwell\ force)/(viscous\ force)=3\mu_0\mu_r m_{1,z}Nl_cI\pi r_{ow}^2\tau_r/2\pi^2\,z_0^4\mu l$ and $\zeta=(Inertial\ force)/(viscous\ force)=ma_z/\mu u_m\pi l$.

The above equations (1.8)(1.10) and (1.9) give rise to three key results. The first, with viscous friction pressure drop governed by the axial position of the magnetic piston; by manipulating the viscous-elastic time scale such that $t^*\gg\tau_d=2(N-1)\tau_r$, the steady-state, i.e., maximal axial displacement, can be postponed for the duration of intermediate continuous operation, reducing energy losses to dissipation. Second, by limiting for $\Delta\mathrm{p}=0$, and $\lambda(t)\to 0$ we simulate the absence of a

destabilizing force. We then substitute $\mathrm{u_m} = \partial\tilde{z}/\partial\mathrm{t}$, $\mathrm{a_z} = \partial^2\tilde{z}/\partial\mathrm{t}^2$, $\tilde{z}(t) = z_0 - A(\partial\tilde{z}/\partial\mathrm{t})t$ and $m = (m_m + m_w)$, where m_m is the mass of the magnet and $m_w = m_{w,pump} + m_{w,tubing}$ being the pump internal fluid mass and setup tubing fluid mass, respectively; if we then reinstitute scaling arguments and solve for τ_r, we obtain a numerical estimate for minimal relay time $\tau_{r,min}$ required to travel the distance z_0 from solenoid-to-solenoid, see Fig, 4b. From it an assessment for max flow rate possible by our system $q_{max} = \left(z_0/\tau_{r,min}\right)\pi(r_m + C)^2$ can then be derived. Above this limit the magnet strips off the solenoid-train due to viscous shear stresses and inertia, inhibiting magnet acceleration. Third and most importantly, Solving (1.10) for Δp, substituting $u_m = q/\pi r_w^2$ and (1.9); then, reinstituting scaling arguments, we obtain the pump pressure evolution $\Delta p(t)$. Integrating over a single pumping duty cycle period τ_d and averaging over time, we obtain the pump performance curve $\Delta p_{,DC}$,

$$\begin{aligned}\Delta p_{,DC} &= -\frac{\mu l}{C^2}\underbrace{\Omega(q)}_{Curve\ slope} \\ &+ \underbrace{\frac{2\pi^2\mu_0\mu_r\tau_r m_{1,z}Nl_cIr_{ow}^2}{Al^2\tau_d z_0^4\epsilon^2}\left(\frac{1}{\left(2A\ arctan\left(cot\left(\frac{\pi\tau_d}{\tau_r}\right)\right)-\pi(A-2)\right)^3}-\frac{1}{8\pi^3}\right)}_{Shut-off\ pressure,\ \ maximum\ pressure\ at\ q=0} \\ &- \underbrace{\frac{ma_z}{2\pi C^2}}_{\substack{Acceleration \\ component}}\end{aligned} \quad (1.11)$$

With the slope $\Omega(q)$ governing the form-function of the performance. The full form of the leading-order solution is provided in SI appendix section A.4.3A.4.4. However, it is of particular interest to examine the asymptotic limit when $\mathrm{t}^*/\mathrm{t}_\nu^* \ll 1$ for which $\Omega(\mathrm{q}) \sim q/\pi\mathrm{r_w^2}\sqrt{1-\left(\underbrace{(a_{\tilde{r}}m\pi\mathrm{r_w^2}-\gamma C\mu q)/C\kappa_f\pi\mathrm{r_w^2}}_{=\lambda_{ss}}\right)^2}$, where λ_{ss} is the steady state eccentric position of the magnetic piston, informing qualitative insights into parameters relations' to performance curve steepness.

4.2. Pump Performance Curve

Characterizing the performance of an existing system requires knowledge of four key parameters $\mu,\ A,\ \kappa_f,\ \gamma$. The effective linear spring coefficient κ_f and dynamic viscosity μ are material properties of the ferrofluid seal; they do not change with the system and are solely governed by the material. Opposite to them: the z-axis coordinate strain $A[1]$ and the center-of-pressure coefficient $\gamma[1]$ are two non-dimensional numbers that are calculated for the specific system based on the shut-off (maximum pressure, no flow) and run-out (maximal flow, no back-pressure); these change with the system limit values. Below we present theoretical and experimental results for the given benchmark system. The dynamic viscosity $\mu = 0.006[Pa\ sec]$ is set constant based on the carrier fluid. The z-axis temporal coordinate strain $A \approx 0.6797[1]$ was derived from (1.11), substituting the shut-off pressure and solving for $A[1]$. The effective linear spring coefficient was experimentally evaluated to be $\kappa_f = 0.667[N\ m^{-1}]$, and last, the center-of-pressure coefficient $\gamma = 2255[1]$ as was calculated from (1.11) substituting $\Delta p_{,DC} = \Delta p = 0, q = q_{max}$ and solving for γ; for more details see SI appendix section A.5.

In Fig. 4a, we plot the evolution of eccentricity $\lambda(T_v)$ over solenoid cycles T_v, in units of solenoid relay time periods, as $z_0 = l$ and $u_m = u_{mag}$. Color transition from dark to light denote an increase in ψ value and respective steady-state flow rate $q_{ss}[ml\ min^{-1}]$. We show in intervals of $|\Delta\lambda_{ss}| = 0.25$ how for $\psi \ll 1$, the value ψ and $|\lambda_{ss}| = |\lambda(\infty)|$ matches; whereas transitioning from $|\lambda_{ss}| \approx 0.75$ to $|\lambda_{ss}| \to 1$ requires a disproportionate increase in ψ and respectively q_{ss}, an attribute of the exponential decay nature of $\lambda(T_v)$ as it approaches its limit at unity.

In Fig. 4b, we compare theoretical approximation to experimental results for the minimal relay time of our experimental setup. With a total accelerated mass $m = (m_m + m_w) \approx 0.009[kg]$, we solve (1.10) for τ_r as discussed in the concluding paragraph of section 4.1 and obtain a theoretical approximate $\tau_{r,min,Theo} = 0.0182[sec]$. Good agreement is seen compared with the experimental minimal relay time $\tau_{r,min,exp} = 0.0188 \pm 0.0007\ [sec]$ at pump run-out; This relay time corresponds to a maximal pumping duty cycle, i.e., the frequency of the magnet to completing an entire pumping

cycle $f_d = 1/\tau_d \approx 4.4 \pm 0.16[Hz]$, at which the maximal flow rate of $q_{max} \approx 320[ml/min]$ is obtained. For more details, see SI appendix A.5.

In Fig. 4c, we focus on the pump performance curve at an unstrained state. We present the experimental data with (solid black) and without (solid red) the ferrofluid coating, showcasing the fluidic seal's merit, without which the pump is rendered useless. Further, reasoning the form of the performance curve, we observe how as flow rate increase from $q_{ss} \approx 50[ml\ min^{-1}]$ (respective to $\psi \approx 1$), to $q_{ss} = q_{max} \approx 320[ml\ min^{-1}]$ (respective to $\psi \approx 6.8$), the diminishing incremental increase in λ to unity compounded with the singularity of the curve slope $\Omega(q) \propto 1/\sqrt{1-\lambda_{ss}^2}$ result in a nonlinear increase in curve gradient; reasoning the form of the performance curve. Good agreement is evident between model prediction (solid blue) and experimental results (solid black) evaluating system performance curve.

Last, in Fig. 4d, we experimentally evaluate pump efficiency $\eta = (Solenoid\ input\ power)/(fluid\ power) = pq_{ss}/V_s I_s$, where $V_s[V]$ and $I_s[A]$ are the voltage and current measured at the solenoid's inlet, respectively. We show current system attain a peak efficiency of $\eta \approx 12.5\%$ at $q_{ss} \approx 225[\mathrm{ml\ min^{-1}}]$ and respective back pressure $\Delta p \approx 6[\mathrm{kPa}]$.

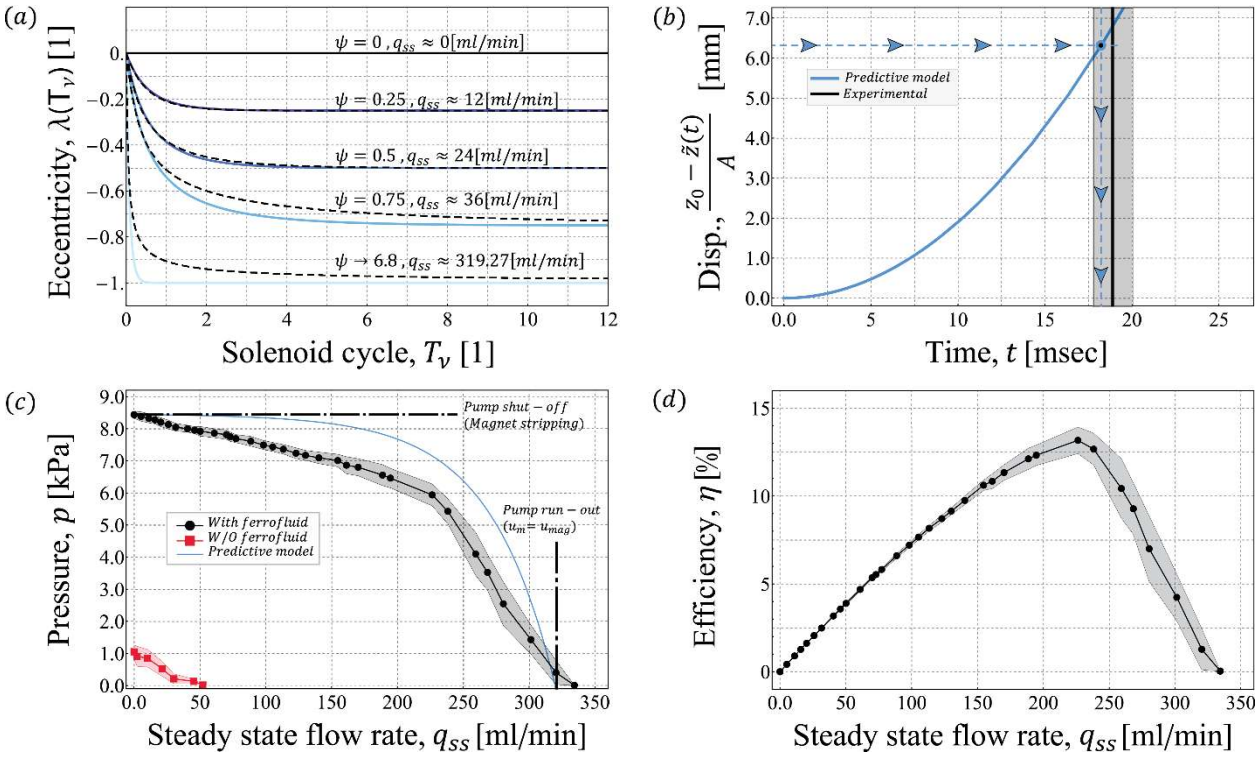

Fig. 4. ***Numerical, experimental, and theoretical results of magnet dynamics and pump performance curve.*** *(a) The time evolution of magnet eccentricity from an initial concentric position (at* $\lambda = 0$*) for different values of* $\psi = \gamma\mu u_m/\kappa_f = \gamma\mu z_0/\kappa_f \tau_r$*, by varying the relay time period* τ_r*. Presented is a quantitative comparison between the numerical solution (dashed black) of the exact expression (1.8) and its explicit leading-order asymptotic approximation (1.9) in solid lines. (b) Comparison of theoretical (pale blue) and experimental (black) minimal relay time* $\tau_{r,min}$*. In pale blue, the solution to equation (1.10) under specified conditions for minimal relay time. The horizontal dashed line represents the distance between one solenoid to the next* $\left(z_0 - \tilde{z}(t)\right)/A = 6.315[mm]$*; the intersecting vertical dashed line informs magnet's minimal travel time. Solid black line indicates the experimental approximation of relay time based on pump run-out,* $\tau_{r,min,exp} = 0.0188 \pm 0.0007\ [sec]$*; Error is determined based on flow sensor specifications. (c) Comparison of theoretical (pale blue) and experimental pump performance curve at unstrained state; with (solid black) and without (solid red) the ferrofluid coating. Marked thresholds indicate pump run-out and shut-off. (d) Experimental characterization of pump efficiency defined* $\eta = (Solenoid\ input\ power)/(fluid\ power) = pq_{ss}/V_s I_s$*, with peak efficiency of* $\eta \approx 12.5\%$ *reached at* $q_{ss} \approx 225[ml\ min^{-1}]$ *(corresponding to a back-pressure* $\Delta p \approx 6[kPa]$ *when intersected with Panel (c)). Error bands for Panels (c) and (d) indicate a 68% confidence (one standard deviation) in the mean based on seven experiments over five separate pumps.*

Several insights and design guidelines emerge from the good agreement between experimental results and the explicit approximation of equation (1.11): the characteristic scale $\beta = (maxwell\ force)/(viscous\ force) = 3\mu_0\mu_r m_{1,z} N l_c I \pi r_{ow}^2 \tau_r / 2\pi^2\, z_0^5 \mu l$ governs design parameter requirements from the individual solenoid coils; such as $\beta \gg 1$ is a sufficient condition to assure the

pump does not stall under the back-pressure generated by the embodied system it drives. $\zeta = (Inertial\ force)/(viscous\ force) = ma_z/\mu u_m \pi l$ and $\varrho = (radial\ accleration)/(Elastic\ forces) = ma_{\tilde{r}}/\kappa_f C$ indicates system susceptibility to external accelerations, and as long as $\zeta \ll 1$ and $\varrho \ll 1$ are maintained, any applied external accelerations to the embodied system will have no appreciable effect on pump performance. The Maxwell pressure $\left|\left(2\pi^2\mu_0\mu_r\tau_r m_{1,z} N l_c I r_{ow}^2/Al^2\tau_d z_0^4\epsilon^2\right)\left(\left(2A\ arctan\left(cot\left(\frac{\pi\tau_d}{\tau_r}\right)\right)-\pi(A-2)\right)^{-3}-1/8\pi^3\right)\right|$ establishes a clear relation between ESP parameters informing parameters to optimize pump pressure, based upon system, material, and geometric restrictions. Finally, the asymptotic pump performance slope $\Omega(\mathrm{q})\sim \mathrm{q}/\pi \mathrm{r}_{\mathrm{w}}^2\sqrt{1-\left((\mathrm{a}_{\tilde{\mathrm{r}}}\mathrm{m}\pi\mathrm{r}_{\mathrm{w}}^2-\gamma\mathrm{C}\mu\mathrm{q})/\mathrm{C}\kappa_{\mathrm{f}}\pi\mathrm{r}_{\mathrm{w}}^2\right)^2}$, qualitatively indicates parameters' relation to curve steepness. To conclude, we thus offer a complete set of guidelines for the design of ESPs using goal-oriented principles.

4.3. Stable Patterns of Taylor-Saffman Instabilities Under Restoring Magnetic Force

Next, we analyze the second mechanism governing our system; correlating the abovementioned prediction with our experiments. In our experimental system, magnet velocity $u_{mag} = z_0/\tau_r$ is held constant, dictated by the constant relay frequency $f_r = 1/\tau_r$; thus the overall flow rate flow would supposedly be maintained at $q_{max} = q_{mag} = u_{mag}\pi r_w^2$. However, flow rate $q[ml\ min^{-1}]$ decay inversely with back-pressure Δp, as predicted by (1.11). We now turn to investigate and reason the means by which a constant velocity-driven positive displacement pump provides a varying flow rate q. Utilizing the equation-based modeling capabilities of COMSOL Multiphysics 5.5, we investigate the 2D flow within a Hele-Shaw cell with a variable height (for more details, see SI section A.6). Based on previous work [76–78], we investigate the emergence of Saffman–Taylor instability, i.e., viscous fingers, along the magnet length. In figure 5, we present a system illustration examining the transient evolution of the ferrofluid seal front from both a 2D top view and 3D projection. Snapshots show the

system at optimal work point at $q_{ss} \approx 225\ [ml\ min^{-1}]$ respective to $\psi = 4.8$ and $|\lambda_{ss}| \to 1$; ferrofluid is denoted in dark gray, pumped fluid in pale blue. In panel (b) we show the emergence of distinct viscous finger structures, the Saffman-Taylor instability; panel (c), viscous fingers complete growth prior to seal breach. Last, in panel (d), we show a stable oscillating viscous finger pattern; starting at $t > O(t^*)[sec]$. The pattern oscillates respective to solenoid train actuation frequency and is maintained over time by force equilibrium between viscous and Maxwell force resultant.

Through this approximate constant cross-section breach in ferrofluid seal – pale blue extension reaching from $z = 0$ to $z = l$, the ESP can maintain continuous operation under varying back-pressure without stalling.

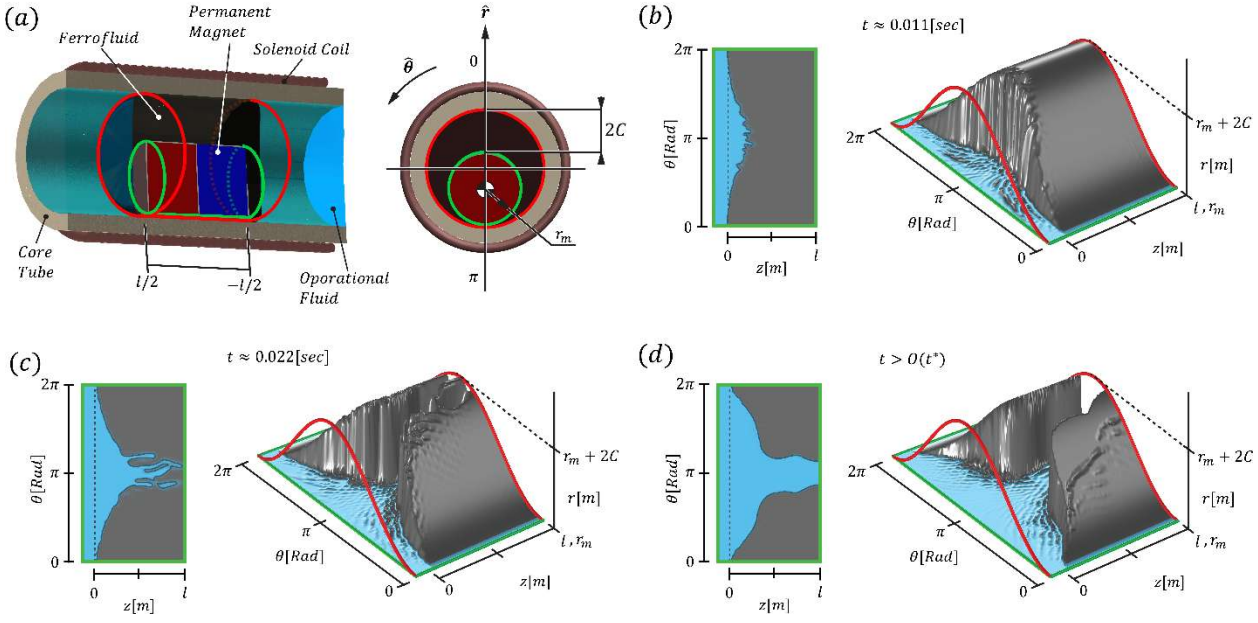

Fig. 5. ***Numerical simulation results for ferrofluid seal dynamics.*** *Presented snapshots examine ferrofluid seal front evolution for the system at optimal work point, $q_{ss} \approx 225\ [ml\ min^{-1}]$ with respective parameters $\psi = 4.8$ and $|\lambda_{ss}| \to 1$. Ferrofluid is denoted by dark gray, pumped fluid in pale blue. (a) Examined configuration illustration showing dimensional notation. The inner core tube diameter (red) and magnet outer diameter (green) are visualized to clarify the coordinate mapping in the subsequent panels. (b) The emergence of distinct viscous fingers (Saffman-Taylor instability) at $t \approx 0.011[sec]$. (c) Snapshot of seal front at $t \approx 0.022[sec]$, viscous fingers complete growth prior to seal breach. (d) The seal front is kept in stable oscillations past $t > O(t^*)[sec]$ by force equilibrium between viscous and Maxwell force resultants'. For the FEM model used in plates (a) through (d), see SI appendix section A.6.*

5. Results

We now turn to demonstrate how the above model predictions and insights emerge in an experimental setup. In Fig. 6, we show the performance curve for an ESP system (constructed within the limitations of our manufacturing capabilities) evolving as we progress strain conditions. In Fig. 6a. and 6b, we present the steady-state performance curves under strained conditions for bending and stretching, respectively (see SI appendix section A.2). It is of particular interest to examine the geometric-mechanical jamming for pump bending deformation. We develop a simplified geometric model to determine the bounding limit for the pump bending strain in relation to geometric parameters or vice versa. Based on our experimental system design, we estimate that mechanical jamming will occur at a bending angle $\phi_{max} \leq 2\arctan(2C_e/(l/2)) \approx 21.5[Deg]$, where C_e is the effective magnet gap at concentric position accounting for magnet rounded corners; for more details, see SI appendix section A.2. We did not find an equivalent mechanical jamming model for tensile strain since failure modes beyond 30% resulted from delamination at the seams, resulting from manufacturing inconsistencies. In Fig. 6a, we see as the pump reaches a bending angle $\phi \approx 20[Deg]$, its performance approaches the point where the run-out and shut-off points intersect where it would seize.

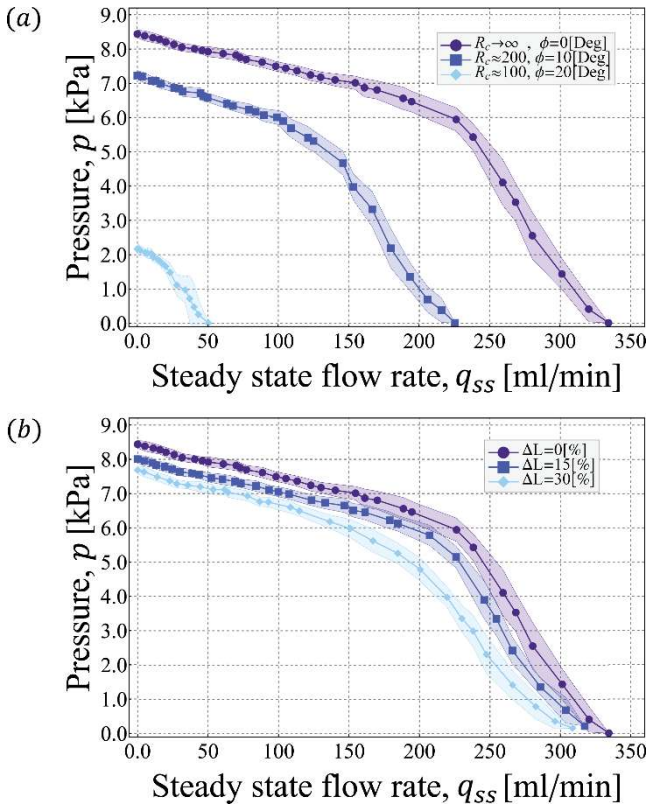

Fig. 6. ***Experimental performance curves of ESP under varying strain conditions.*** *Error bands indicate a 68% confidence (one standard deviation) in the mean based on seven experiments over five separate pumps; plot markers represent the experimental mean value. (a) Experimental pump performance curve at unstrained* $\phi = 0[Deg]$ *and strained states* $\phi = 10{,}20[Deg]$*. (b) Experimental pump performance curve at free state* $\Delta\ell/\ell_0 = 0 = 0[\%]$ *and axially stretched* $\Delta\ell/\ell_0 = 0.15, 0.3 = 15, 30[\%]$.

In Fig. 7, we present a conceptual vision for functionality. Our design implements an ESP as an apparatus incorporated into a same-scale compliant boat that is forced through an obstruction course that includes 15% lateral contraction and 20-degree bends. The boat then emerges at the other end of the course and propels itself forward via the jet generated by the ESP (similarly to the free jet visualized in Fig. 2f).

We quantify the non-dimensional strain rate to be $\dot{E} = (\Delta\ell/\ell_0)/(\Delta t/t^*) = O(10^{-2})$[1], and normalize based on the viscous elastic time scale. We thus relate the strain rate to the governing mechanisms discussed above and in the Analysis section 4; allowing us to expand the conclusions regarding performance, mechanical jamming, and hysteresis beyond the proposed scale of this study. Data used to evaluate strain rate $\dot{E}$, is available at SI appendix section A.7 Table A.2.

Initially, we push the embodiment through the obstruction course using the semi-rigid outlet tube as a flexible pushrod with both inlet and outlet tubes connected. During deployment stages $7b(I) \rightarrow 7b(IV)$ we continuously log both pressure and flow rate. In Fig. 7a, we illustrate the experimental setup; inset illustrates a focused top view of the embodiment structure with top-level components. Fig. 7b shows the deployment stage (left panel): (I) starting point at rest, (II) squeezing through a 15% lateral contraction, (III) 20-degree positive bend, (IV) 20-degree negative bend. During $(II) \rightarrow (III)$, $(III) \rightarrow (IV)$ and past (IV), system reverts to an unstrained state. Next, we present the start and end positions of the self-propulsion stage (right panel), where the system completes a swimming task, using a free jet for propulsion (as visualized in Fig. 2g and Movie S1). In Fig. 7c, we present the real-time performance of the ESP during dynamic deformation. The non-hysteretic nature of the ESP is evident upon returning to the unstrained state in sections $(II) \rightarrow (III)$, and past (IV); the pressure difference past section (IV) corresponds to change in elevation $\Delta p = \rho g h = 1000 \cdot 9.81 \cdot 0.10 \approx 1[kPa]$. A real-time video of the system navigating the course is available; see Movie S5, S6.

Last, we offer an avenue for using the ESP apparatus as a self-sensor to estimate its strained state defined as $\varphi = \varepsilon_{eqv}/\varepsilon_{max} = \phi_{eqv}/\phi_{max} \leq 1$ and provide a warning mechanism prior to mechanical jamming. Correcting for back-pressure from the external load, we can plot the dynamic work-point, i.e. pressure and flow rate at a point in time, and overlay on Fig. 6a; we can then estimate the equivalent bending ϕ_{eqv} and calculate the strained state ratio φ, where $\varphi = 1$ indicates the system jamming limit. In Fig. 7c, boxed region A ($q \approx 180[ml\,min^{-1}], p \approx 3.1[kPa]$) has an equivalent strain $\phi_{eqv} \approx 10[Deg]$ respective to a strained state of $\varphi = 0.46$; whereas regions B ($q \approx 40[ml\,min^{-1}], p \approx 1.4[kPa]$) and C ($q \approx 23[ml\,min^{-1}], p \approx 1.4[kPa]$) correspond with the equivalent strain $\phi_{eqv} \approx 20[Deg]$ for a strained state of $\varphi = 0.93$, informing proximity to pump stalling.

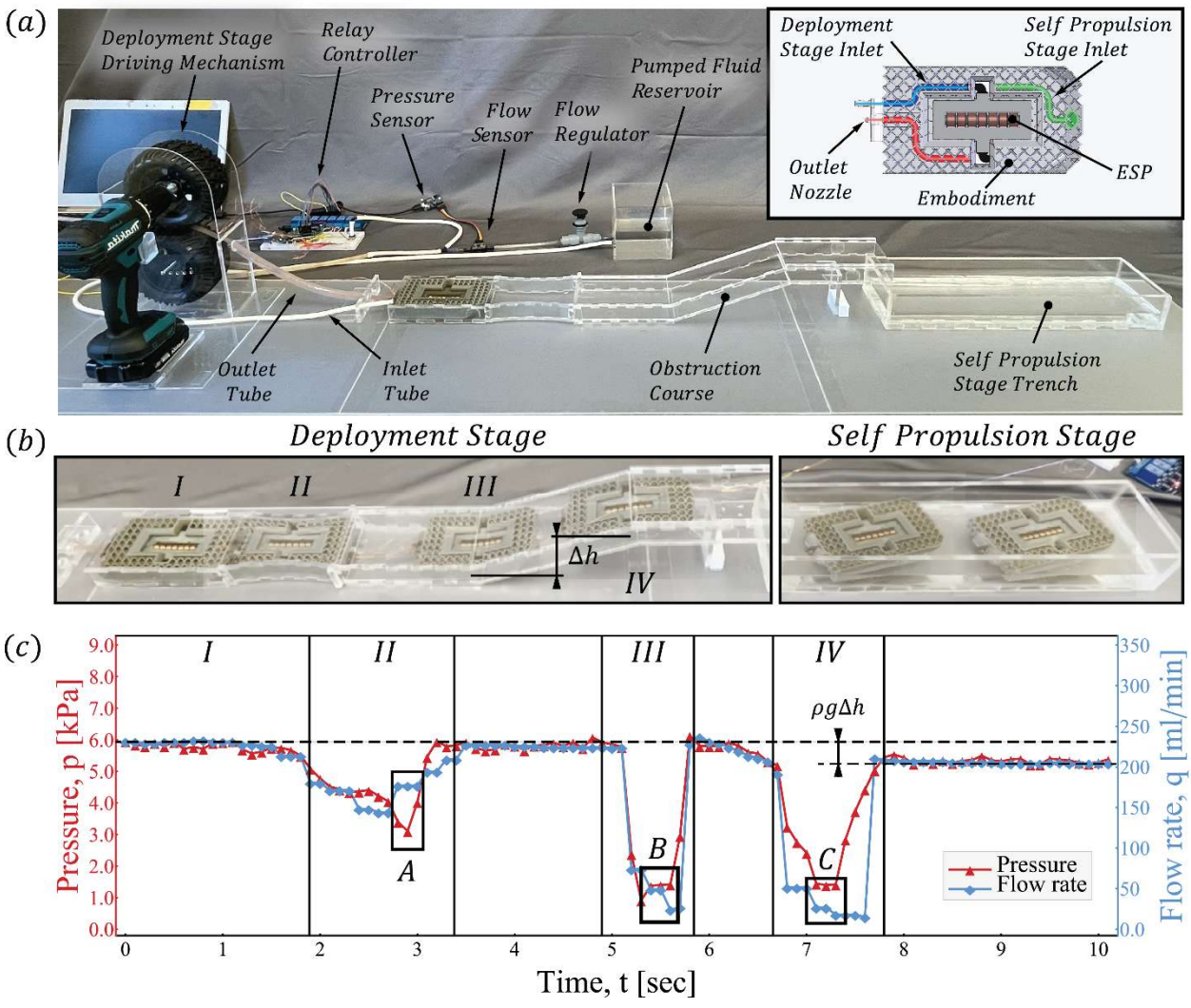

Fig. 7. ***Experimental setup demonstrating an ESP integrally embodied in a soft robotic apparatus.*** *The embedded ESP endures axial and angular strain while providing continuous fluid pressure and flow rate before eventually emerging at the far end. It then completes a swimming task using free jet propulsion (See jet visualization, Movie S1). (a) Experimental setup, inset illustrates a focused top view of the embodiment structure with key top-level components. (b) Deployment stage (left) - Snapshot sequence of embodiment at various stages during deployment: (I) starting point at rest, (II) lateral deformation squeezing through a 15% contraction, (III) 20-degree positive bend, (IV) 20-degree negative bend, during (II)→(III), (III)→(IV) and past (IV) system reverts to an unstrained state. Self-propulsion stage (right) – start and end positions of self-propulsion post-deployment. (c) Continuous dynamic performance plotted in real-time during deformation with evaluated non-dimensional strain rate* $\dot{E} = (\Delta\ell/\ell_0)/(\Delta t/t^*) = O(10^{-2})[1]$. *Boxed regions A,B and C are regions of interest where we use the ESP for self-sensing to estimate its strained state* $\varphi = \varepsilon_{eqv}/\varepsilon_{max} = \phi_{eqv}/\phi_{max} \leq 1$*; thus providing a warning method prior to mechanical jamming, which occurs at* $\varphi = 1$. *Boxed region A (*$q \approx 180[\text{ml min}^{-1}]$, $p \approx 3.1[\text{kPa}]$*) has an equivalent strain of* $\varphi = 0.46$*; whereas regions B (*$q \approx 40[\text{ml min}^{-1}]$, $p \approx 1.4[\text{kPa}]$*) and C (*$q \approx 23[\text{ml min}^{-1}]$, $p \approx 1.4[\text{kPa}]$*) correspond to a strained state of* $\varphi = 0.93$.

6. Concluding Remarks

In this work, we tackle the leading component standing in the way of soft robotic systems from functioning under deformation - the pump. We present a simple, focused experimental demonstration and a theoretical framework, showing for the first time an elastomeric solenoid-driven pump (denoted ESP) undergoing deformations of its own length scale $O(10^{-2})[m]$ while generating pressures and flow rates in the order of $O(10^5)[Pa]$ and $O(10^2)[ml\,min^{-1}]$ for a power consumption of $O(10^{-1})[W]$. The resulting work-point is the largest reported for pumps that operate under large deformations (of its own length scale) with no appreciable hysteresis.

We observe two governing physical mechanisms in these systems: magnetohydrodynamic levitation and the Saffman-Taylor instability in the presence of a restoring magnetic force. In addition, we report the characteristic scales and an explicit leading-order predictive model detailing how the proposed governing mechanism of magnetohydrodynamic lubrication is scalable with respect to pressure, flow rate, size, and radius of curvature.

Last, we elucidate a list of avenues for tailoring performance in goal-oriented design: We show how the restoring force centering the magnetic piston and the maximal pressure generated by the pump are inversely proportional to the magnet-wall gap squared; evident by the characteristic pressure scale $p^* \propto 1/C^2$. We relate ferrofluid's effective dynamic viscosity μ and linear spring coefficient κ_f to the

destabilizing force acting on the magnetic piston; whereby in making $\psi \propto \mu/\kappa_f \ll 1$ we reduce steady-state eccentricity $|\lambda_{ss}|$ and with it viscous friction - the leading order source of dissipative energy loss. We point to a criterion over the non-dimensional numbers ζ and ϱ, the inertial to viscous force ratios, such that when $\zeta \ll 1$ and $\varrho \ll 1$, external accelerations exerted on the pump will have no appreciable effect on performance. We provide minimal criteria sufficient to assure the pump does not stall under the back-pressure, so long that the non-dimensional number β, the Maxwell to viscous force ratio, $\beta \gg 1$. We show the ESP apparatus as a sensor to estimate its own strained state, defined $\varphi = \varepsilon_{eqv}/\varepsilon_{max} \leq 1$, and provide a warning mechanism prior to mechanical jamming due to excessive deformation. Last, we inform how by manipulating the viscous-elastic time scale to be greater than the pumping duty cycle $t^* \gg \tau_d$We can delay the magnetic piston from stabilizing at steady-state maximal eccentricity during operation, further reducing energy loss and dissipation.

Combined, these provide an explicit set of scaling laws - a toolbox to assist in goal-oriented design; a first step towards developing a practical deformable pump that will serve as the foundation for future advances in soft-pump technology.

7. Acknowledgments

This work was sponsored by the Army Research Laboratory and was accomplished under Cooperative Agreement (CA) W911NFT16T2T0008, Air Force Office of Scientific Research, Contract: FA9550-20-1-0254, and Office of Naval Research, Contract: N00014-20-1-2438.

The views and conclusions contained in this document are those of the authors and should not be interpreted as representing the official policies, either expressed or implied, or the Army Research Laboratory or the US Government. The US Government is authorized to reproduce and distribute reprints for Government purposes notwithstanding any copyright notation herein.

8. Author Contributions

R.F.S., N.L, H.S.A. and Y.M conceived the research subject. H.S.A. and Y.M. constructed the experimental setup, conducted the experiments, and analyzed the experimental data. Y.M. Conceived and performed the theoretical analysis and numerical computations. Both Y.M and H.S.A contributed

equally and have the right to list their name first in their CV. All authors contributed to the article and approved the submitted version.

9. Competing Financial Interests

The authors declare no competing financial interests.

10. References

1. Suzumori, K., Iikura, S. & Tanaka, H. Development of flexible microactuator and its applications to robotic mechanisms. in 1622,1623,1624,1625,1626,1627-1622,1623,1624,1625,1626,1627 (IEEE Computer Society, 1991). doi:10.1109/ROBOT.1991.131850.
2. Suzumori, K., Koga, A., Kondo, F. & Haneda, R. Integrated flexible microactuator systems. *Robotica* **14**, 493–498 (1996).
3. Tondu, B. & Lopez, P. Modeling and control of McKibben artificial muscle robot actuators. *IEEE Control Systems Magazine* **20**, 15–38 (2000).
4. Suzumori, K., Endo, S., Kanda, T., Kato, N. & Suzuki, H. A Bending Pneumatic Rubber Actuator Realizing Soft-bodied Manta Swimming Robot. in *Proceedings 2007 IEEE International Conference on Robotics and Automation* 4975–4980 (2007). doi:10.1109/ROBOT.2007.364246.
5. Shepherd, R. F. *et al.* Multigait soft robot. *PNAS* **108**, 20400–20403 (2011).
6. Ilievski, F., Mazzeo, A. D., Shepherd, R. F., Chen, X. & Whitesides, G. M. Soft Robotics for Chemists. *Angewandte Chemie International Edition* **50**, 1890–1895 (2011).
7. Shepherd, R. F., Stokes, A. A., Nunes, R. M. D. & Whitesides, G. M. Soft Machines That are Resistant to Puncture and That Self Seal. *Advanced Materials* **25**, 6709–6713 (2013).
8. Deimel, R. & Brock, O. A compliant hand based on a novel pneumatic actuator. in *2013 IEEE International Conference on Robotics and Automation* 2047–2053 (2013). doi:10.1109/ICRA.2013.6630851.
9. Meller, M. A., Bryant, M. & Garcia, E. Reconsidering the McKibben muscle: Energetics, operating fluid, and bladder material. *Journal of Intelligent Material Systems and Structures* **25**, 2276–2293 (2014).
10. Tolley, M. T. *et al.* A Resilient, Untethered Soft Robot. *Soft Robotics* **1**, 213–223 (2014).

11. Mosadegh, B. *et al.* Pneumatic Networks for Soft Robotics that Actuate Rapidly. *Advanced Functional Materials* **24**, 2163–2170 (2014).

12. Peele, B. N., Wallin, T. J., Zhao, H. & Shepherd, R. F. 3D printing antagonistic systems of artificial muscle using projection stereolithography. *Bioinspir. Biomim.* **10**, 055003 (2015).

13. Mac Murray, B. C. *et al.* Poroelastic Foams for Simple Fabrication of Complex Soft Robots. *Advanced Materials* **27**, 6334–6340 (2015).

14. Argiolas, A. *et al.* Sculpting Soft Machines. *Soft Robotics* **3**, 101–108 (2016).

15. Zatopa, A., Walker, S. & Menguc, Y. Fully Soft 3D-Printed Electroactive Fluidic Valve for Soft Hydraulic Robots. *Soft Robotics* **5**, 258–271 (2018).

16. Drotman, D., Jadhav, S., Sharp, D., Chan, C. & Tolley, M. T. Electronics-free pneumatic circuits for controlling soft-legged robots. *Science Robotics* **6**, (2021).

17. Nagarkar, A. *et al.* Elastic-instability–enabled locomotion. *Proc Natl Acad Sci USA* **118**, e2013801118 (2021).

18. Tolley, M. T. *et al.* A Resilient, Untethered Soft Robot. *Soft Robotics* **1**, 213–223 (2014).

19. Aubin, C. A. *et al.* Electrolytic vascular systems for energy-dense robots. *Nature* **571**, 51–57 (2019).

20. Cacucciolo, V. *et al.* Stretchable pumps for soft machines. *Nature* **572**, 516–519 (2019).

21. Diteesawat, R. S., Helps, T., Taghavi, M. & Rossiter, J. Electro-pneumatic pumps for soft robotics. *Science Robotics* **6**, eabc3721 (2021).

22. Cao, C., Gao, X. & Conn, A. T. A Magnetically Coupled Dielectric Elastomer Pump for Soft Robotics. *Advanced Materials Technologies* **4**, 1900128 (2019).

23. Stergiopulos, C. *et al.* A Soft Combustion-Driven Pump for Soft Robots. in (American Society of Mechanical Engineers Digital Collection, 2014). doi:10.1115/SMASIS2014-7536.

24. Tang, W. *et al.* Customizing a self-healing soft pump for robot. *Nature Communications* **12**, 2247 (2021).

25. Jahanshahi, A., Axisa, F. & Vanfleteren, J. Fabrication of a biocompatible flexible electroosmosis micropump. *Microfluid Nanofluid* **12**, 771–777 (2012).

26. Kawun, P., Leahy, S. & Lai, Y. A thin PDMS nozzle/diffuser micropump for biomedical applications. *Sensors and Actuators A: Physical* **249**, 149–154 (2016).

27. Tanaka, Y., Noguchi, Y., Yalikun, Y. & Kamamichi, N. Earthworm muscle driven bio-micropump. *Sensors and Actuators B: Chemical* **242**, 1186–1192 (2017).

28. Wehner, M. *et al.* An integrated design and fabrication strategy for entirely soft, autonomous robots. *Nature* **536**, 451–455 (2016).

29. Onal, C. D., Chen, X., Whitesides, G. M. & Rus, D. Soft Mobile Robots with On-Board Chemical Pressure Generation. in *Robotics Research* (eds. Christensen, H. I. & Khatib, O.) vol. 100 525–540 (Springer International Publishing, 2017).

30. Olsson, A., Enoksson, P., Stemme, G. & Stemme, E. Micromachined flat-walled valveless diffuser pumps. *Journal of Microelectromechanical Systems* **6**, 161–166 (1997).

31. Jang, L.-S. *et al.* A stand-alone peristaltic micropump based on piezoelectric actuation. *Biomed Microdevices* **9**, 185–194 (2007).

32. Lei, K. F. *et al.* A vortex pump-based optically-transparent microfluidic platform for biotech and medical applications. *Proc Inst Mech Eng H* **221**, 129–141 (2007).

33. Mac Murray, B. C. *et al.* Poroelastic Foams for Simple Fabrication of Complex Soft Robots. *Advanced Materials* **27**, 6334–6340 (2015).

34. Richter, A., Plettner, A., Hofmann, K. A. & Sandmaier, H. A micromachined electrohydrodynamic (EHD) pump. *Sensors and Actuators A: Physical* **29**, 159–168 (1991).

35. Ahn, S.-H. & Kim, Y.-K. Fabrication and experiment of a planar micro ion drag pump. *Sensors and Actuators A: Physical* **70**, 1–5 (1998).

36. Chen, C.-H. & Santiago, J. G. A planar electroosmotic micropump. *Journal of Microelectromechanical Systems* **11**, 672–683 (2002).

37. Zengerle, R., Ulrich, J., Kluge, S., Richter, M. & Richter, A. A bidirectional silicon micropump. *Sensors and Actuators A: Physical* **50**, 81–86 (1995).

38. Homsy, A., Linder, V., Lucklum, F. & de Rooij, N. F. Magnetohydrodynamic pumping in nuclear magnetic resonance environments. *Sensors and Actuators B: Chemical* **123**, 636–646 (2007).

39. Ashouri, M., Shafii, M. B. & Moosavi, A. Theoretical and experimental studies of a magnetically actuated valveless micropump. *J. Micromech. Microeng.* **27**, 015016 (2016).

40. Van de Pol, F. C. M., Van Lintel, H. T. G., Elwenspoek, M. & Fluitman, J. H. J. A thermopneumatic micropump based on micro-engineering techniques. *Sensors and Actuators A: Physical* **21**, 198–202 (1990).

41. Sim, W. Y., Yoon, H. J., Jeong, O. C. & Yang, S. S. A phase-change type micropump with aluminum flap valves. *J. Micromech. Microeng.* **13**, 286–294 (2003).

42. Jung, J.-Y. & Kwak, H.-Y. Fabrication and testing of bubble powered micropumps using embedded microheater. *Microfluid Nanofluid* **3**, 161–169 (2007).

43. Shaegh, S. A. M. *et al.* Plug-and-play microvalve and micropump for rapid integration with microfluidic chips. *Microfluid Nanofluid* **19**, 557–564 (2015).

44. Zhou, M. *et al.* Miniaturized soft centrifugal pumps with magnetic levitation for fluid handling. *Sci. Adv.* **7**, eabi7203 (2021).

45. Chang, H. S., Chi, C. Q. & Zhao, P. Z. A theoretical and experimental study of ferrofluid lubricated four-pocket journal bearings. *Journal of Magnetism and Magnetic Materials* **65**, 372–374 (1987).

46. Osman, T. A., Nada, G. S. & Safar, Z. S. Static and dynamic characteristics of magnetized journal bearings lubricated with ferrofluid. *Tribology International* **34**, 369–380 (2001).

47. Osman, T. A., Nada, G. S. & Safar, Z. S. Different Magnetic Models in the Design of Hydrodynamic Journal Bearings Lubricated with Non-Newtonian Ferrofluid. *Tribology Letters* **14**, 211–223 (2003).

48. Montazeri, H. Numerical analysis of hydrodynamic journal bearings lubricated with ferrofluid. (2007).

49. Kuzhir, P. Free boundary of lubricant film in ferrofluid journal bearings. *Tribology International* **41**, 256–268 (2008).

50. van der Wal, K., van Ostayen, R. A. J. & Lampaert, S. G. E. Ferrofluid rotary seal with replenishment system for sealing liquids. *Tribology International* **150**, 106372 (2020).

51. Moskowitz, R. Technology ferrofluids: Liquid magnetics: A space-age research spin-off finds its way out of the laboratory and into a host of lubricating and damping applications. *IEEE Spectrum* **12**, 53–57 (1975).

52. Kumar, D., Sinha, P. & Chandra, P. Ferrofluid squeeze film for spherical and conical bearings. *International Journal of Engineering Science* **30**, 645–656 (1992).

53. Lampaert, S. G. E. Planar Ferrofluid Bearings: Modelling and Design Principles. (2015).

54. Lampaert, S., Spronck, J. & van Ostayen, R. Load and stiffness of a planar ferrofluid pocket bearing. *Proceedings of the Institution of Mechanical Engineers, Part J: Journal of Engineering Tribology* **232**, 14–25 (2018).

55. Boots, A. S. T., Krijgsman, L. E., de Ruiter, B. J. M., Lampaert, S. G. E. & Spronck, J. W. Increasing the load capacity of planar ferrofluid bearings by the addition of ferromagnetic material. *Tribology International* **129**, 46–54 (2019).

56. Park, G. S. & Park, S. H. Design of magnetic fluid linear pump. *IEEE Transactions on Magnetics* **35**, 4058–4060 (1999).

57. Hatch, A., Kamholz, A. E., Holman, G., Yager, P. & Bohringer, K. F. A ferrofluidic magnetic micropump. *Journal of Microelectromechanical Systems* **10**, 215–221 (2001).

58. Hartshorne, H., Backhouse, C. J. & Lee, W. E. Ferrofluid-based microchip pump and valve. *Sensors and Actuators B: Chemical* **99**, 592–600 (2004).

59. Yamahata, C. & Gijs, M. A. M. Plastic micropumps using ferrofluid and magnetic membrane actuation. in *17th IEEE International Conference on Micro Electro Mechanical Systems. Maastricht MEMS 2004 Technical Digest* 458–461 (2004). doi:10.1109/MEMS.2004.1290621.

60. Kurtoğlu, E. *et al.* Ferrofluid actuation with varying magnetic fields for micropumping applications. *Microfluid Nanofluid* **13**, 683–694 (2012).

61. Michelson, T., Rudnick, J., Baxter, J. & Rashidi, R. A Novel Ferrofluid-Based Valve-Less Pump. in *Volume 7: Fluids Engineering* V007T08A009 (American Society of Mechanical Engineers, 2019). doi:10.1115/IMECE2019-10790.

62. Lampaert, S. G. E., Fellinger, B. J., Spronck, J. W. & van Ostayen, R. A. J. In-plane friction behaviour of a ferrofluid bearing. *Precision Engineering* **54**, 163–170 (2018).

63. Paggi, M., Amicarelli, A. & Lenarda, P. SPH Modelling of Hydrodynamic Lubrication along Rough Surfaces. *Lubricants* **7**, 103 (2019).

64. Sfyris, D. & Chasalevris, A. An exact analytical solution of the Reynolds equation for the finite journal bearing lubrication. *Tribology International* **55**, 46–58 (2012).

65. Leal, L. G. *Advanced Transport Phenomena: Fluid Mechanics and Convective Transport Processes*. (Cambridge University Press, 2007).

66. Beschorner, K. E., Higgs, C. F. & Lovell, M. R. Derivation of Reynolds Equation in Cylindrical Coordinates Applicable to Pin-on-Disk and CMP. in 399–401 (American Society of Mechanical Engineers Digital Collection, 2009). doi:10.1115/IJTC2008-71245.

67. Chen, X., Li, F., Haidak, G., Wang, D. & Li, S. Characterizations of the oil film considering the elastohydrodynamic lubrication effect of the piston–cylinder interface. *AIP Advances* **10**, 095017 (2020).

68. Hedman, D. & Fjellström, M. *Modeling the interactions between magnetic particles*. (2013).

69. Grant, I. S. & Phillips, W. R. *Electromagnetism*. (John Wiley & Sons, 2013).

70. David J. Griffiths. *Introduction to Electrodynamics*.

71. Campbell, P. *Permanent Magnet Materials and their Application*. (Cambridge University Press, 1996).

72. Landecker, P. B. & Villani, D. D. AN ANALYTIC SOLUTION FOR THE TORQUE BETWEEN TWO MAGNETIC DIPOLES. 5.

73. Ravaud, R., Lemarquand, G., Babic, S., Lemarquand, V. & Akyel, C. Cylindrical Magnets and Coils: Fields, Forces, and Inductances. *IEEE Transactions on Magnetics* **46**, 3585–3590 (2010).

74. Robertson, W., Cazzolato, B. & Zander, A. Axial Force Between a Thick Coil and a Cylindrical Permanent Magnet: Optimizing the Geometry of an Electromagnetic Actuator. *IEEE Transactions on Magnetics* **48**, 2479–2487 (2012).

75. Ku, J. G., Liu, X. Y., Chen, H. H., Deng, R. D. & Yan, Q. X. Interaction between two magnetic dipoles in a uniform magnetic field. *AIP Advances* **6**, 025004 (2016).

76. Coutinho, A. L. G. A. & Alves, J. L. D. Finite element simulation of nonlinear viscous fingering in miscible displacements with anisotropic dispersion and nonmonotonic viscosity profiles. *Computational Mechanics* **23**, 108–116 (1999).

77. Zimmerman, W. B. & Homsy, G. M. Nonlinear viscous fingering in miscible displacement with anisotropic dispersion. *Physics of Fluids A: Fluid Dynamics* **3**, 1859–1872 (1991).

78. Holzbecher, E. Modeling of Viscous Fingering. 6.

79. Horne, R. N. & Rodriguez, F. Dispersion in tracer flow in fractured geothermal systems. *Geophysical Research Letters* **10**, 289–292 (1983).

80. G. I. Taylor. Dispersion of soluble matter in solvent flowing slowly through a tube. *Proc. R. Soc. Lond. A* **219**, 186–203 (1953).

Supplementary Information for

Magnetohydrodynamic Levitation for High-Performance Flexible Pumps.

Yoav Matia†, Hyeon Seok An, Robert F. Shepherd, Nathan Lazarus

†**To whom correspondence should be addressed; E-mail:** ym279@cornell.edu

This PDF file includes:

Supplementary text

Table A.1, A.2.

Figs. S1. to S12.

Other supplementary materials for this manuscript include the following:

Movie S1 - Visualization of pump performance generating free jet.

Movie S2 - Ultrasound evaluation of minimal solenoid relay time.

Movie S3 - Numerical investigation of viscous fingers, 2D top view.

Movie S4 - Numerical investigation of viscous fingers, 3D projection.

Movie S5 - Experimental demonstration of ESP integral embodiment, deployment stage.

Movie S6 - Experimental demonstration of ESP integral embodiment, self-propulsion stage.

Contents

Appendix A

A.1. Table 1 - Comparison of Systems from Different Technologies and Scales.

Ref††	Compliant material	Deformable (Reported preformance under deformation)	Pumping principle	Run-out, Max. flow rate [ml min^{-1}]	Shut-off, Max. pressure [kPa]	Pump volume [cm^3]
25.	Y	N	Electroosmotic	0.0012	0.01	0.01
33.	N	N	Electrohydro dynamic (EHD)	14.	0.42	0.01
41.	N	N	Thermopneumatic	0.01	0.49	0.05
40.	N	N	Phase change	0.0061	0.1	0.072
34.	N	N	Electrohydro dynamic (EHD)	0.055	0.1	0.09
27.	Y	N	Electromagnetic diffuser	0.135	0.245	0.095
36.	N	N	Electrostatic	0.16	29.	0.098
37.	N	N	Magnetohydrodynamics	0.0015	0.18	0.16
29.	N	N	Piezoelectric diffuser	2.3	74.	0.26
20.	Y	Y	Electrohydro dynamic (EHD)	6.	14.	1.2
30.	N	N	Piezoelectric	0.0368	0.52	2.
28.	Y	N	Bio-microactuator	0.005	0.17	3.2
38.	N	N	Electrohydro dynamic (EHD)	0.7	0.75	3.2
31.	N	N	Rotery pump, radial impeller	9.5	8.	3.5
24.	Y	N	Positive Ion migration	423.	9.2	3.6
42.	N	N	Diaphragm-pneumatic	0.082	0.41	6.
35.	N	N	Electroosmotic	0.015	33.	9.
44.	Y	N	Monopropellant decomposition	6.4	50.	9.1
39.	N	N	Electro-thermopneumatic	0.03	5.1	9.2
43.	Y	N	Magnetic levitation	33.7	0.297	12.
22.	N	N	MCDEA (Mag. Coupled DEA)	800.	3.	13.
This study	Y	Y	Elastomeric Solenoid-driven pump (ESP)	325.	8.	23.
23.	Y	N	Combustion	40.	60.	49.
21.	Y	N	Electro-pneumatic	161.	2.34	49.
45.	N	N	Monopropellant decomposition	11.	24.1	130.
32.	Y	N	Pneumatic	430.	12.	500.

[1] Data presented herein is based on information reported or derived implicitly via images and figures when no such information was provided explicitly. Accordingly, some data may vary by a factor. However, great care was taken to ensure that the critical parameters associated with a given system are identified to properly position it in the correct scale.

TABLE. A.1. ***Characterization of performance for comparable state-of-the-art pumping solutions[1], used in figure 1.***

A.2. Experimental System Design and Setup.

A.2.1. Fabrication Process of the ESP.

The proprietary urethane methacrylate resin was a proprietary formulation (UMA 90, Carbon 3D, Inc.) 3D-printed on a Carbon 3D M1 printer. UMA 90 was used to fabricate coil guides. We then wind a copper wire (diameter: $250\ [\mu m]$) at a winding density of $N = 5760\ [Coils/m]$. In order to control the magnet piston, seven coils sheath the center tube of the ESP. A cylindrical neodymium magnet (N52, length: $6.315\ [mm]$, diameter: $4\ [mm]$) is inserted into a center tube (diameter: $4.5\ [mm]$, length: $50\ [mm]$). Sealing the gap ($250\ [\mu m]$) between the core center tube and the neodymium magnet, we use FerroTec, EFH1 ferrofluid to coat the magnet, creating a liquid seal. Due to the magnetic field from the permanent magnet, i.e., the magnetic piston core, ferrofluid is automatically localizing around and is transported with the piston core during pumping operation.

The silicone-urethane resin was a proprietary formulation (SIL 30, Carbon 3D, Inc.) 3D-printed on a Carbon 3D M1 printer. Three parts of the ESP pump were 3D-printed (the top, bottom, and center tube). The 3D-printed parts were thermally cured in the oven ($8\ [hr]$ at $120\ [°C]$). Four stainless steel balls (diameter: $\approx 3.5[mm]$) were placed at the one-way ball valve area (see main text, section 2, Fig. 2c). The same SIL 30 was used to glue the top and bottom ESP parts. SIL 30 is placed at the bottom part and covered by the top part; we then put it in the oven for gluing ($8\ [hr]$ at $120\ [°C]$). The center tube is then glued at the center of the ESP part by using SIL 30 and thermally cured in the oven again.

A.2.2. ESP Performance Measurement.

To measure the ESP performance, a regulator, flowmeter (Renesas, FS2012-1020-NG), and pressure sensor (Honeywell Sensing and Productivity Solutions, SSCDANN030PAAA5) are required. Fig. 2b (see main text, section 2) shows the connection between these three components. The flowmeter and regulator are connected in serial after the pump outlet. A Y-connector is used between the pump outlet and the flowmeter to connect the pressure sensor. In order to control the regulator based on the setup, we measured the flow rate and pressure in real-time. In order to measure the performance of ESP,

we measured pressure and flow rate from the fully closed state of the regulator to the fully open state by gradually opening the regulator. Based on the viscous-elastic characteristic time scale $t^* \sim \pi l \mu / \epsilon^2 \kappa_f$ (see derivation section A.4.3) we calculate the system achieving steady-state after a time scale of the order $t^* \approx 0.113[sec]$. To assure we have achieved steady-state prior to collecting data, we allow the system one minute to stabilize. We take pressure sensor readings and evaluate flow rate using both a flowmeter and by collecting the outlet spillage for two minutes in a $1000[ml]$ glass beaker; then normalize for water density at room temperature.

A.2.3. Performance Curve Characterization Under Strained Conditions.

We 3D printed a bending jig and a tensile strain stage to measure the ESP performance under deformation (bending, tensile strain). In Fig. S1a, we present schematics and definition of the bending angle $\phi[deg]$ and radius of curvature $R_c[m]$. In Fig. S1b, we show the ESP attached to the bending Jigs, each with a fixed radius of curvature $R_c \to \infty\ (flat)$, $R_c = 200\ [mm]$, and $R_c = 100\ [mm]$. The bend radius of curvature $R_c = 200\ [mm]$ and $R_c = 100\ [mm]$ corresponds to $\phi = 10[Deg]$ and $\phi = 20[Deg]$ bending angle, respectively. The bent ESP performance was measured using the same setup and method as detailed in section A.2.2.

To test the ESP performance under tensile strain (i.e., stretching), we mounted the 3D printed stretching stage on a linear stage. ESPs were attached to the stretching stage and stretched while the linear stage was operating, as shown in Fig. S2. We stretched the ESP up to 30% ($\Delta\ell/\ell_0 = 0.3$), and the performance was measured for every 10% increase in tensile strain, see Fig. S2b.

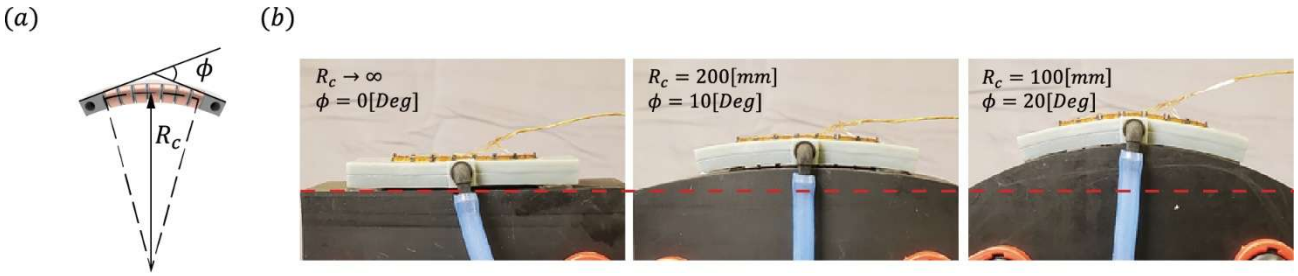

Fig. S1. ***Experimental setup for ESP performance curve characterization, bending strain.*** *(a) Schematic illustration of measuring the radius of curvature R_c and bending angle ϕ. (b) Photos of the ESP bent on the bending stage with different curvatures.*

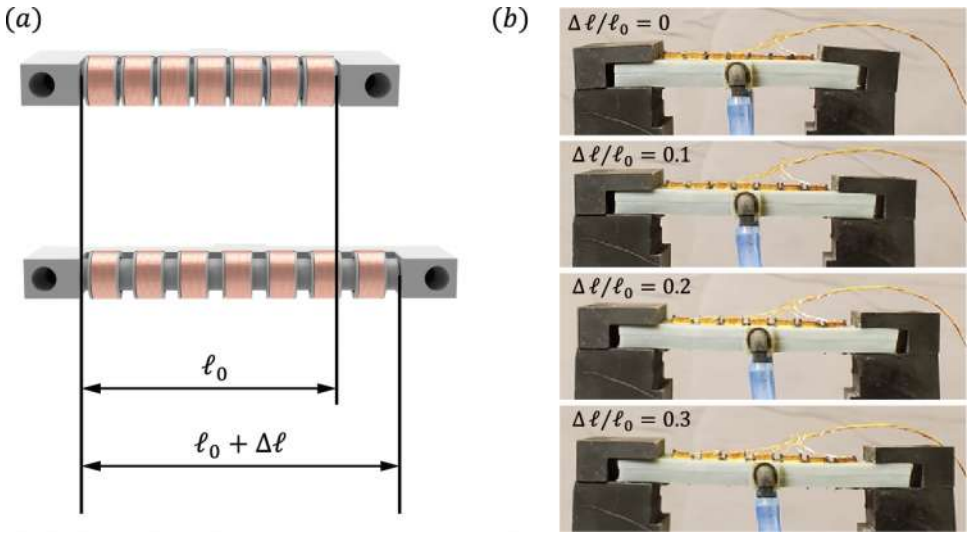

Fig. S2. ***Experimental setup for ESP performance curve characterization, tensile strain.*** *(a) schematic illustration of measuring the tensile strain (ε). (b) Photos of the ESP stretched on the stretching stage with different tensile strains.*

A.3. Geometrical Model for Characterizing Geometrical Jamming Under Bending.

This section presents a simplified geometric model to determine the bounding limit for pump bending strain in relation to geometric parameters, see figure S3. We assume mechanical jamming occurs when the magnet exhausts its radial travel and is now pressed against the inner wall of the core tube (in light brown); resulting in columbic friction then bringing it to a halt upon contact. We do not consider the driving maxwell force's ability to overcome coulombic friction, driving the magnetic core past the point of mechanical contact. Figure S3a presents an illustrative view of our experimental observation, where at leading-order, the solenoid coil assemblies acting as vertebrae govern the core tube curvature. Therefore, we propose a simplified deformed state form-function using a discrete two rigid link model, see Fig. S3b.

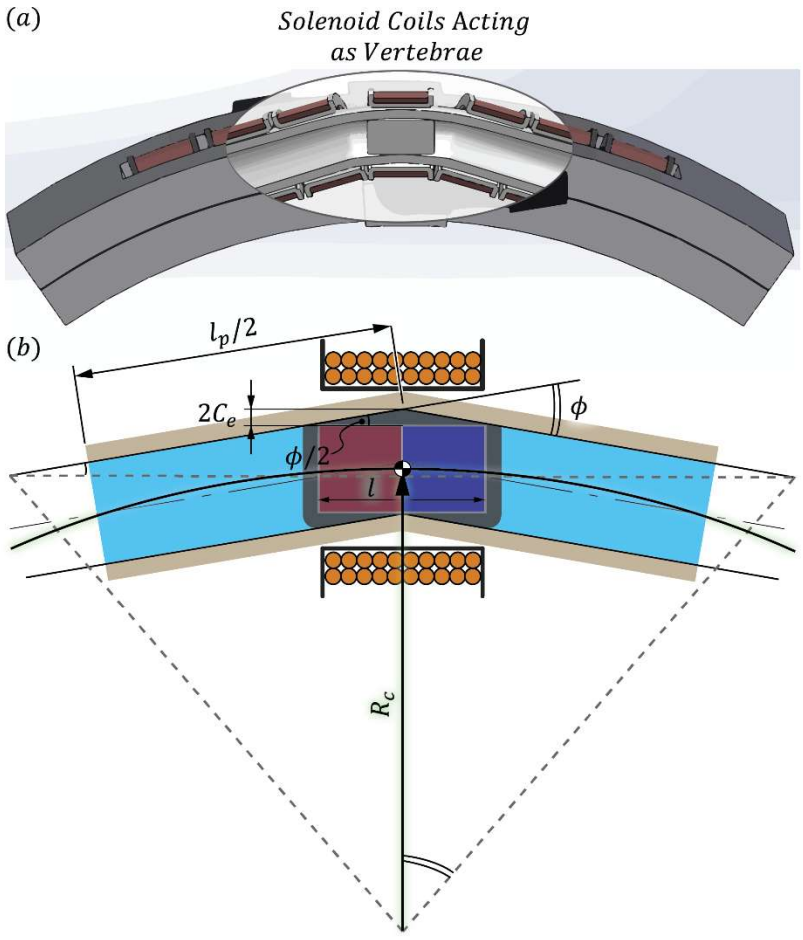

Figure. S3. ***Geometrical Model for characterization of geometrical jamming under bending.*** *(a) Illustrative view of our experimental observation, where the solenoid coil assemblies are acting as vertebrae govern the core tube curvature. (b) A simplified discrete two-link model for the deformed state form-function under bending illustrated at mechanical jamming.*

Based on this simplified geometric model, we formulate our geometric mechanical jamming condition,

$$\phi_{max} \leq 2\arctan\left(\frac{2C_e}{l/2}\right) \approx 21.5[Deg]\,, \tag{A.1}$$

where $C_e = C + r_{m,fillet} = 0.25[mm] + 0.05[mm] = 0.3[mm]$ is the effective increase to magnet-wall gap at the concentric position. Doing so, we take into account the magnet's reduced effective radius (thus increase in the gap) due to its filleted corners of radius $r_{m,fillet}$. Having formulated the two-link bending angle ϕ_{max}, we can now formulate the geometric relation for the pump's radius of curvature at jamming,

$$R_{c,min} = \frac{l_p}{2}\sin\left(\frac{\phi}{2}\right) + \frac{\frac{l_p}{2}\cos\left(\frac{\phi}{2}\right)}{\tan(\phi)} - (2C + r_m) \approx 94[mm] \tag{A.1}$$

Where $l_p = 0.072[m]$ is the total pump length.

A.4. Lubrication model, Fluid Field Pressure, and Velocity Profile Solutions.

We formulate a predictive model characterizing the steady-state and dynamic performance of an ESP; It consists of a cylindrical elastomeric core tube inside which viscous pressure and maxwell forces levitate a magnetic core coated with ferrofluid. The ferrofluid coating provides a seal that maintains its integrity as the pump deforms during operation. In addition, the viscous pressure generated within its fluidic field, resulting from the forward motion of the magnet, maintains the underlying magnetohydrodynamic levitation, preventing the solid core from coming in contact with the wall and jamming. Fig. S4 illustrates the modeled geometry. Panel (a) illustrate the axial cross-section of the proposed system. Panels (b) and (c) illustrate the magnet axial degrees of freedom; panel (d) shows system geometry definitions used in the cylindrical-to-gap curvilinear coordinate mapping. Last, panel (e) presents a qualitative illustration of the ferrofluid flow field surrounding the magnet due to the superimposed pressure-driven (Hagen-Poiseuille), and shear-driven (Couette) flows. The external coil surrounding the core tube was omitted for visual clarity in panels $(b) - (e)$.

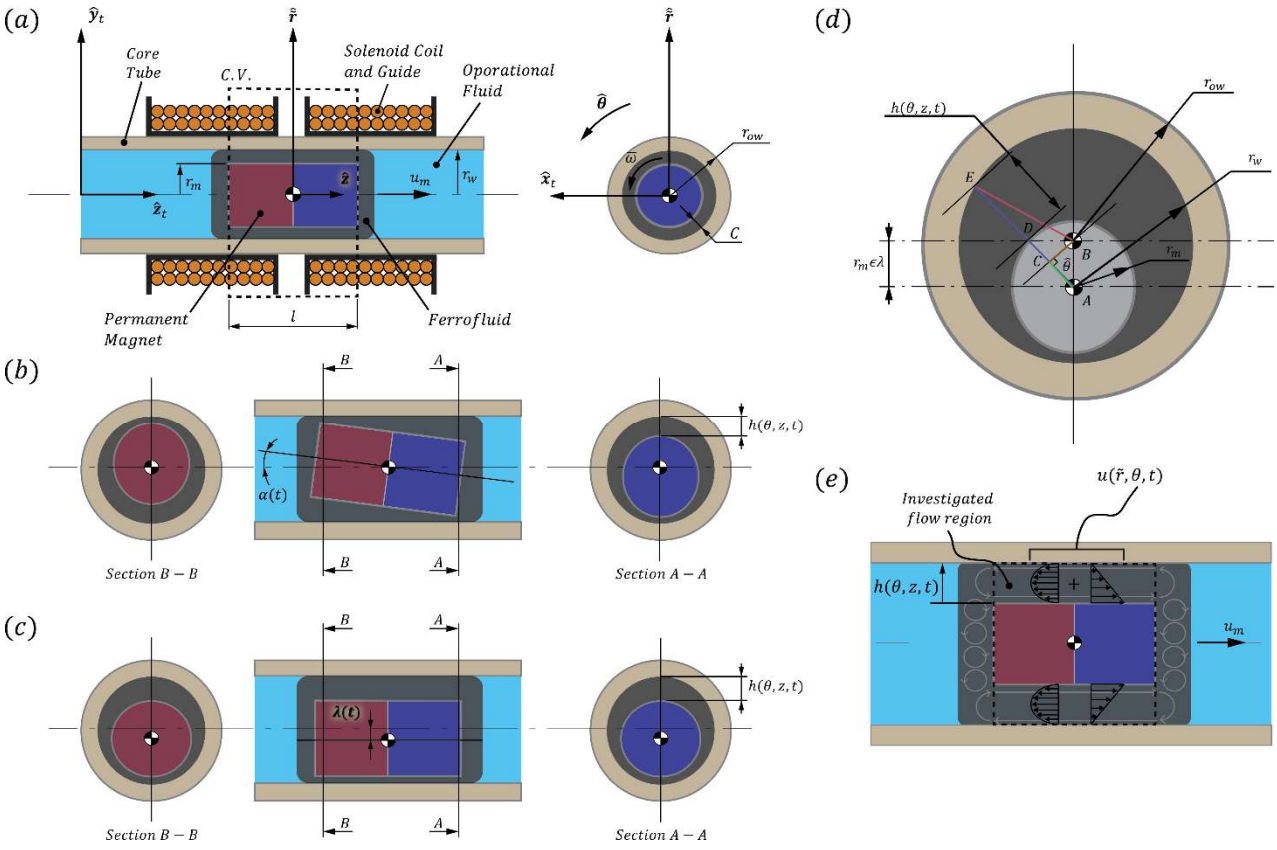

Figure. S4. ***System schematic Geometry and section views for visual clarity.*** *(a) System axial cross-section with the magnetic core axially centered. (b) Illustrating angular deviation of the magnetic core from a coaxial position. (c) Illustration of respective parallel deviation. For plates (b) and (c), the Solenoid coil surrounding the core tube was omitted for visual clarity. (d) illustration of system geometric definitions used in the Magnetic piston-to-gap curvilinear coordinate mapping. (e) Qualitative illustration of ferrofluid flow field surrounding magnet due to superimposed pressure-driven (Hagen-Poiseuille) and shear-driven (Couette) flows. The external coil surrounding the tube in panels (b)-(e) were omitted for visual clarity.*

We define vector variables using bold letters, direction vectors by hat notation, non-dimensional variables by capital letters, characteristic values by an asterisk, and superscript (n) denoting the nth order of magnitude. We define a curvilinear frame $(\hat{\boldsymbol{x}}_t, \hat{\boldsymbol{y}}_t, \hat{\boldsymbol{z}}_t)$ following the curvature of the encasing core tube (inner radius $r_w[m]$ and external radius $r_{ow}[m]$), where $\hat{\boldsymbol{z}}_t$, it the direction tangent to the core tube axis, and $\hat{\boldsymbol{x}}_t$ the bi-normal parallel to the horizon. We define a moving, gap-curvilinear cylindrical frame $(\hat{\boldsymbol{r}}, \hat{\boldsymbol{\theta}}, \hat{\boldsymbol{z}})$ centered at the magnet center of mass; the magnet has a radius $r_m[m]$, a length $l[m]$ and a mass $m[kg]$. We assign the gap height coordinate $\tilde{r} = r - r_m$ ranging from $[0, h(\theta, z, t)]$, where $r[m]$ is the radius from the cylindrical moving frame (panel (e) segment $\overline{AE}$) and $h(\theta, z, t)[m]$ is gap height (panel (e) segment $\overline{DE}$). We define the deviation of the magnet axis from the tube axis by

$\lambda(z,t)[1] = \lambda_{||}(t) - z/(l/2)\tan\big(\alpha(t)\big)$, Where $\lambda_{||}(t)[1]$ is the ratio of the parallel shift to the ideal gap width $C[m]$, and the second term stands for the $\hat{\boldsymbol{z}}$ axis dependence of the gap as resulting from the tilting of the magnet by angle $\alpha(t)[rad]$ as a function of time. We define $\Delta p_{pump}[Pa]$ as the pressure drop across the magnet along the $\hat{\boldsymbol{z}}$ axis from end to end. The magnet is traveling at a velocity $u_m = z_0/\tau_d$ where $z_0[m]$ is the distance between the centers of the magnetic moment of the permanent magnet $\boldsymbol{m_1}[J/T]$ and solenoid coil $\boldsymbol{m_2}[J/T]$, and $\tau_d = 1/f_d$ is the duty cycle period for the successive coil actuation at frequency $f_d[Hz]$. Each coil is characterized by: the number of turns per unit meter $N[1/m]$ assuming a single layer winding, the permeability of free space $\mu_0[N/A^2]$, the relative permeability $\mu_r[1]$ in the effective volume where the magnetic field is in effect, and the current flowing through it $I[A]$. External forces acting on the magnet include the dipole-dipole interaction $\boldsymbol{f}_{b,2\to1}[N]$, gravity's acceleration $\boldsymbol{g} = (g_r, 0, g_z)[m/s^2]$, and the rheological influences of the ferrofluid due to viscous friction formulated by dynamic viscosity $\mu[Pa\cdot s]$ and the distributed magnetic volume force modeled using a linear spring model and coefficient $\kappa_f[N/m]$.

In Fig. S4d, we determine the magnet-wall gap $h(\theta,z,t)$; we define the gap using a moving coordinate system translating with the inside cylinder, i.e., the magnetic piston core,

$$\begin{aligned} h(\theta,z,t) = r_w - r_m = \underset{gap\ curvlinear\ coordinate}{Gap\ measure\ in} = \overline{DE} = \overline{AE} - \overline{AD} \\ = r_m\epsilon\lambda\cos\theta + \sqrt{\big(r_m(1+\epsilon)\big)^2 - (r_m\epsilon\lambda)^2 + (r_m\epsilon\lambda\cos\theta)^2} - r_m\,, \end{aligned} \tag{A.2}$$

where $\epsilon = C/l{\sim}C/r_m \ll 1$ our system's small parameter, with $C[m]$ and $l[m]$ standing for magnet-wall gap at the concentric position, and the magnet length respectively. We limit axial eccentricity by the magnet-wall gap for both parallel $\lambda(t) \le C$, and angular misalignment $(\alpha(t)l)/2 \le C$; core tube radial and axial dimensions do not deform due to fluid pressure, and both tube and magnetic piston core do not rotate.

In the narrow gap between the magnetic piston and the bounding tube wall, we consider the internal flow of ferrofluid to be one-phase, Newtonian, and incompressible as the magnet is driven forward. Next, we set our normalized variables and coordinates,

$$U_z = \frac{u_z[m/sec]}{u_m}\,, \qquad U_\theta = \frac{u_\theta[m/sec]}{u_r^*}\,, \qquad U_r = \frac{u_r[m\backslash sec]}{u_r^*},$$
$$Z = \frac{z}{l}\,, \qquad R = \frac{\tilde{r}}{C} \sim \frac{\tilde{r}}{l\epsilon}\,, \qquad T_v = \frac{t}{t_v^*} = \frac{u_m\, t}{l}\;, \quad T = \frac{t}{t_f^*} \tag{A.3}$$
$$H = \frac{h}{C} \sim \frac{h}{l\epsilon}\;, \qquad P = \frac{p}{p^*}\;, \quad \Delta P_{pump} = \frac{\Delta p_{pump}}{p^*}\;.$$

We note that the angular coordinate θ and the magnet eccentricity $\lambda(z,t)$ are intrinsically non-dimensional and require no additional normalization.

The fluid motion within the gap is governed by the momentum and mass equations under the lubrication approximation,

$$\hat{R}\colon \frac{\partial P^{(0)}}{\partial R} = 0\;, \qquad \widehat{\Theta}\colon \frac{\partial P^{(0)}}{\partial \Theta} = 0\;, \qquad \hat{Z}\colon 0 = -\frac{\partial P^{(0)}}{\partial Z} + \frac{\partial^2 U_z^{(0)}}{\partial R^2}\;,$$
$$and\;\; \frac{\partial U_r^{(0)}}{\partial R} + \frac{\partial U_z^{(0)}}{\partial Z} = 0\,, \tag{A.4}$$

with emergent characteristic scales for pressure $p^* \sim \mu u_m / l\epsilon^2$ and ferrofluid kinematics $\epsilon \sim C/l \sim C/r_m \sim u_r^*/u_m$ from order-of-magnitude analysis. Next, we Set our system's boundary and initial conditions. In dimensional form, these are: the magnetic core translates axially $u_r(\tilde{r}=0,\theta,z,t) = -\frac{\partial h}{\partial t}$, but does not rotate $u_\theta(\tilde{r}=0,\theta,z,t) = \bar{\omega} = 0$, as the magnet is driven forward at $u_z(\tilde{r}=0,\theta,z,t) = u_m$; the enveloping tube (i.e., core tube) is at rest $u_r(\tilde{r}=h,\theta,z,t) = 0$, $u_\theta(\tilde{r}=h,\theta,z,t) = 0$, $u_z(\tilde{r}=h,\theta,z,t) = 0$, and the entire system starts from rest $u_r(\tilde{r},\theta,z,t=0) = 0$, $u_\theta(\tilde{r},\theta,z,t=0) = 0$, $u_z(\tilde{r},\theta,z,t=0) = 0$. With these defined, we then substitute scaling arguments and begin by solving the $\hat{Z}$-axis equation to gain the axial velocity profile inside the ferrofluid gap in non-dimensional form,

$$U_z^{(0)} = \underbrace{\frac{1}{2}\frac{\partial P^{(0)}}{\partial Z}(R^2 - HR)}_{\substack{hagen-poiseuille \\ flow}} \underbrace{-\frac{R}{H} + 1}_{Couette\ flow}\;. \tag{A.5}$$

Substituting (A.5) into the continuity equation from (A.4) and solving for the gap radial direction, we obtain,

$$U_r^{(0)} = -\frac{1}{12}\frac{\partial^2 P^{(0)}}{\partial Z^2}(2R^3 - 3HR^2 + H^3) + \frac{1}{4}\frac{\partial P^{(0)}}{\partial Z}\frac{\partial H}{\partial Z}(R^2 - H^2) + \frac{1}{2}\frac{\partial H}{\partial Z}\left(1 - \frac{R^2}{H^2}\right). \tag{A.6}$$

Implementing the magnetic core axial translation boundary condition,

$$U_r(R = 0, \Theta, Z, T_v) = -\frac{\partial H}{\partial T_v}\ , \qquad u_r^* = \epsilon u_m \tag{A.7}$$

We attain a special form of the Reynolds equation from general lubrication theory,

$$-\frac{\partial H}{\partial T_v} = \underbrace{-\frac{1}{12}\frac{\partial^2 P^{(0)}}{\partial Z^2}(H^3) - \frac{1}{4}\frac{\partial P^{(0)}}{\partial Z}\frac{\partial H}{\partial Z}(H^2)}_{-\frac{1}{12}\frac{\partial}{\partial Z}\left(\frac{\partial P^{(0)}}{\partial Z}(H^3)\right)} + \frac{1}{2}\frac{\partial H}{\partial Z}, \tag{A.8}$$

where in leading order,

$$H^{(0)} = \lambda(Z, T_v)\cos\Theta + 1 + O(\epsilon^2)$$
$$\lambda(z,t)[1] = \underbrace{\lambda_{||}(t)[1]}_{\substack{Change\ due\ to \\ parallel \\ shift}} \underbrace{-\frac{z[m]}{l/2[m]}\tan\big(\alpha(t)\big)}_{\substack{Change\ due \\ to\ tilt}}. \tag{A.9}$$

Substituting we write,

$$H^{(0)} = 1 + \left(\underbrace{\lambda_{||}(T_v)[1]}_{\substack{Change\ due\ to \\ Parallel \\ shift}} \underbrace{-2Z\tan\big(\alpha(T_v)\big)}_{\substack{change\ due \\ to\ tilt}}\right)\cos\Theta\,, \tag{A.10}$$

limiting for the case of small tilt angles $\alpha(t) \ll 1$ as $C \ll l$,

$$H^{(0)}(\Theta, T_v) = 1 + \underbrace{\lambda_{||}(T_v)}_{\substack{Change\ due\ to \\ Parallel \\ shift}}\cos\Theta\,. \tag{A.11}$$

Substituting, and integrating twice over Z, as $H^{(0)} \neq H^{(0)}(Z)$ as the change due to tilt was rendered negligible,

$$P^{(0)}(\Theta, Z, T_v) = \frac{12\cos\Theta}{\big(1 + \lambda_{||}(T_v)\cos\Theta\big)^3}\frac{\partial\lambda_{||}(T_v)}{\partial T_v}\left(\frac{Z^2}{2} - \frac{1}{8}\right) + \Delta P_{pump}\left(Z + \frac{1}{2}\right). \tag{A.12}$$

Substituting (A.12) back to (A.5), we obtain the $\hat{Z}$-axis velocity component in non-dimensional form,

$$U_z^{(0)}(R,\Theta,Z,T_\nu) = \underbrace{\frac{1}{2}\left(\frac{12\cos\Theta}{\left(1+\lambda_{||}(T)\cos\Theta\right)^3}\frac{\partial\lambda_{||}(T)}{\partial T_\nu}Z+\Delta P_{pump}\right)\left(R^2-H^{(0)}R\right)}_{\substack{hagen-poiseuille\\ flow}} \underbrace{-\frac{R}{H^{(0)}}+1}_{Couette\ flow}. \quad \text{(A.13)}$$

Observing the above pressure (A.12) profile, two key insights crucial to understanding the underlying physics of ESP systems become evident. First, we point to the pressure scaling in our system $p^*{\sim}\mu u_m/l\epsilon^2$, from which it is evident that we are to expect very large pressure gradients of the order $O(1/\epsilon^2)$ respective to wall-magnet gap. Second, we note the nonlinearity related to the product of eccentric $\lambda_{||}(T)$ and its transient $\partial\lambda_{||}(T)/\partial T_\nu$, as evident by the pressure equation (A.13); specifically, its circumferential asymmetric distribution, where high pressures concentrate where the magnetic core nears the wall. Figure S5a shows the circumferential uniform pressure in the case of a concentric magnetic core, whereas Fig. S5b and S5c show the development of the asymmetry in the pressure profile as it translates from a concentric position.

With these insights combined, it becomes evident that any deviation from the concentric position will generate a non-proportional increase in pressure of the order of $O(1/\epsilon^2)$ focused at the narrowing gap; resulting in a lift force to restore the magnetic core to concentric position. This self-correcting mechanism of Magnetohydrodynamic levitation (magneto, as Maxwell forces are employed to drive the magnetic piston), constitutes the underlying physics responsible for offsetting the destabilizing effect of the back-pressure Δp the magnetic piston, acting as an inverted pendulum. Absent of this mechanism, any back-pressure acting on the pump will bring the magnetic piston to contact the wall; the resulting contact then introduces coulomb friction, leading to increased energy losses to dissipation and subsequent reduction in efficiency and performance, and may eventually lead to stalling the pump entirely.

Above, we discuss the importance of the circumferential pressure gradient in generating force equilibrium and stopping the magnet core from coming into contact with the wall. Next, we examine the importance of eccentricity on pump performance. To do so, we examine the axial velocity profiles (A.13), specifically, the balance between the pressure-driven Hagen-Poiseuille flow term and the shearing Couette flow. This balance, required to uphold mass conservation, governs the emergence of

the necessary secondary backflow near the wall when the magnet-wall gap narrows, generating steep near-wall velocity gradients, as is evident in figure S6(a-c). Considering energy dissipation is proportional to the spatial velocity gradient near the wall $\Delta E_{loss} \propto shear\ stress \propto (\partial U_z/\partial R)|_{R=0}$; ideally, we would want to optimize the lift pressure in our system based on pressure scale parameters respective to our system's characteristic back-pressure. Doing so ensures our system will maintain a position as close as possible to concentric, reducing viscous friction to a minimum and optimizing performance.

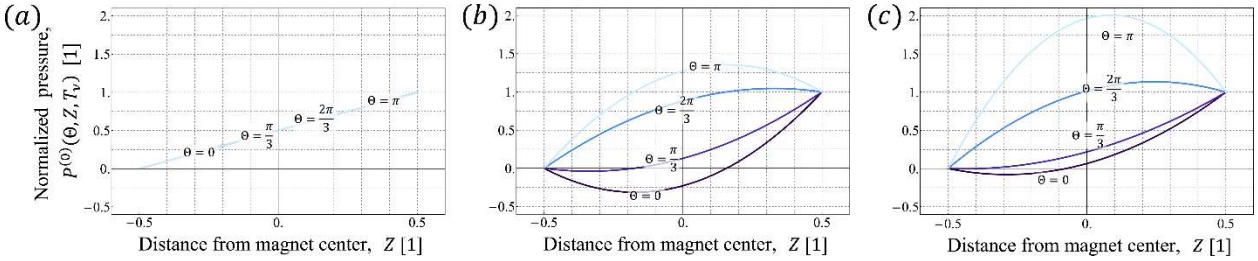

Fig. S5. ***Snapshot view of ferrofluid internal pressure field*** $\mathbf{P^{(0)}}$ ***as the ferrofluid plug is transported with the permanent magnetic core for the case of*** $\boldsymbol{\Delta P_{pump} = 1}$. *(a) for* $\lambda = 0$, $\partial\lambda_{||}/\partial \mathrm{T}_\nu = 0$. *(b) for* $\lambda = 0.01$, $\partial\lambda_{||}/\partial \mathrm{T}_\nu = 0.5$. *(c) for* $\lambda = 0.2$, $\partial\lambda_{||}/\partial \mathrm{T}_\nu = 0.5$. *The color gradient of solid lines indicates respective values of* $\Theta = 0, \pi/3, 2\pi/3, \pi$ *respectively.*

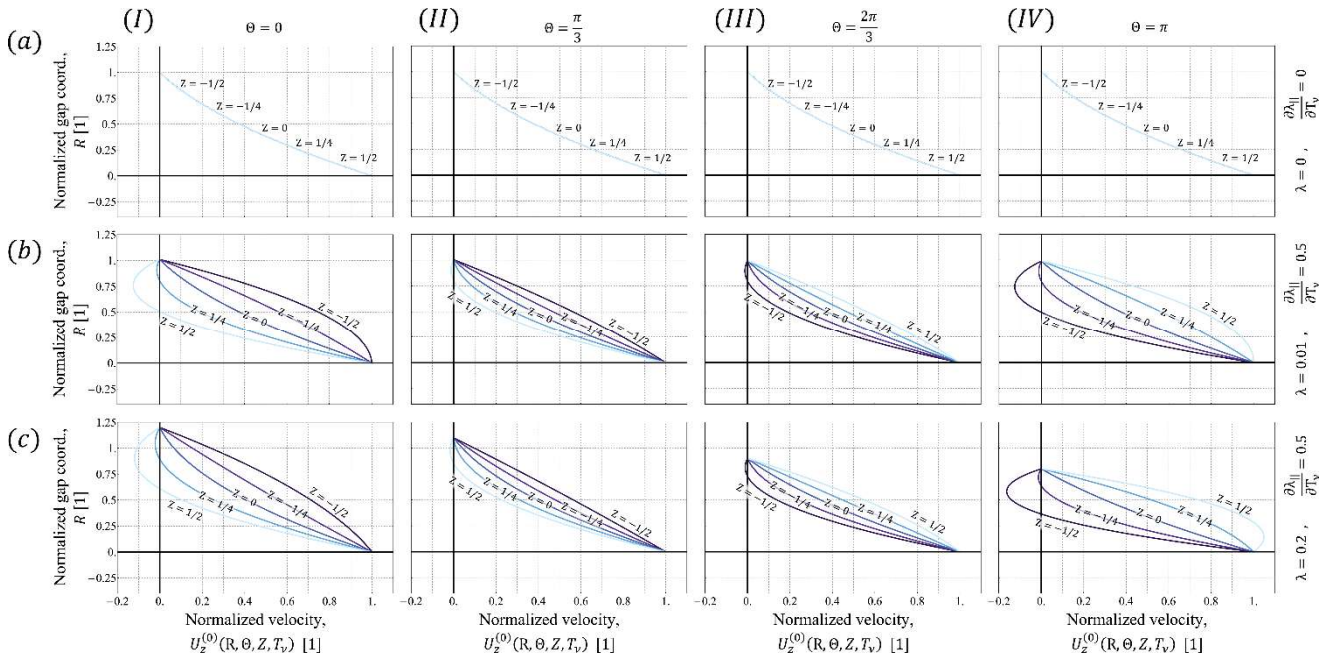

Fig. S6. ***Snapshot views in time of ferrofluid axial velocity*** $\mathbf{U_z^{(0)}}$ ***as ferrofluid plug is being transported with the permanent magnetic core for the case of*** $\boldsymbol{\Delta P_{pump} = 1}$. *(a) for* $\lambda = 0$, $\partial\lambda_{||}/\partial \mathrm{T}_\nu = 0$. *(b) for* $\lambda = 0.01$, $\partial\lambda_{||}/\partial \mathrm{T}_\nu = 0.5$. *(c) for* $\lambda = 0.2$, $\partial\lambda_{||}/\partial \mathrm{T}_\nu = 0.5$. *Column I-IV*

correspond to the local profile at angle $\theta = 0, \pi/3, 2\pi/3, \pi$ *respectively. The transition from blue to red indicates the local velocity profile along* $Z = -1/2, -1/4, 0.1/4, 1/2$, *respectively.*

A.4.1. Viscous Pressure Forces.

This section focuses on calculating the system's resistance to the magnetic core forward travel. Resistance to this motion comes from both pressure drag (hydrostatic terms), and friction drag (the stress tensor's deviatoric terms). From the pressure field $p^{(0)}(\theta, z, t)$ perspective, we address friction drag. We have a core of length $l[m]$ that moves inside a tube, with fluid filling the gap between the magnetic core and the wall,

$$f_z^{(\mu)} = \int_0^{2\pi} \left(\int_{-l/2}^{l/2} \underbrace{\mu \left(\underbrace{\frac{\partial u_z^{(0)}}{\partial \tilde{r}}}_{\tau_{rz}=\tau_{zr}} \right)\Bigg|_{\tilde{r}=0}}_{\substack{shear\ stress \\ at\ the\ wall}} dz \right) l\epsilon d\theta \,. \tag{A.14}$$

From a force balance perspective, we address the pressure drag. We have a pressure gradient between the back and front of the piston, resulting from the external load as the magnetic piston core separates high and low potential fluid,

$$f_z^{(p)} = -\pi (l\epsilon)^2 \Delta p, \tag{A.15}$$

with Δp the external load back-pressure imposed on the pump relative to the inlet reservoir.

Last, we have the pressure force in the radial direction, mentioned in the closing argument of section A.4 and visualized in Fig. S5; this is the viscous pressure resulting from the magnetohydrodynamic lubrication acting as a restoring force centering the core,

$$f_{\tilde{r}}^{(p)} = \underbrace{\left(\int_0^{2\pi} \int_{-l/2}^{l/2} -p^{(0)} \cos(\theta)\, dz\, l\epsilon d\theta \right) \cos(\beta)}_{\substack{axial\ Pressure\ lift \\ force}} . \tag{A.16}$$

A.4.2. Magnet-Solenoid Leading-Order Model for Dipole-Dipole Interaction.

This section addresses the magnetic force, i.e., Maxwell force, resulting from the dipole-dipole interaction of the magnetic piston core (i.e., permanent magnet) and the solenoid coils. We assume both magnetization effects (mutual induction) and the finite volume effects (the deviation of magnet

geometry from spherical magnet uniformly magnetized) are negligible compared to the leading order approximation of a point like dipole-dipole interaction. Limiting the case of $\alpha \ll 1$ such that the magnetic core remains parallel to the $\hat{z}$-axis during its travel in the core tube, we propose Ampere's model [68–75], and formulate the magnetic dipole maxwell force,

$$\underbrace{\boldsymbol{f}_{b,1\to 2}}_{\substack{is\ the\ force\ by\\ magnetic\ field\ 1\\ acting\ on\ 2}} = +\frac{3\mu_0\mu_r|\boldsymbol{m_1}||\boldsymbol{m_2}|}{4\pi|\tilde{\boldsymbol{c}}|^4}\Big(\hat{\tilde{\boldsymbol{c}}}(\hat{\boldsymbol{m}}_{\boldsymbol{1}}\cdot\hat{\boldsymbol{m}}_{\boldsymbol{2}}) + \hat{\boldsymbol{m}}_{\boldsymbol{1}}\big(\hat{\tilde{\boldsymbol{c}}}\cdot\hat{\boldsymbol{m}}_{\boldsymbol{2}}\big) + \hat{\boldsymbol{m}}_{\boldsymbol{2}}\big(\hat{\tilde{\boldsymbol{c}}}\cdot\hat{\boldsymbol{m}}_{\boldsymbol{1}}\big) - 5\hat{\tilde{\boldsymbol{c}}}\big(\hat{\tilde{\boldsymbol{c}}}\cdot\hat{\boldsymbol{m}}_{\boldsymbol{1}}\big)\big(\hat{\tilde{\boldsymbol{c}}}\cdot\hat{\boldsymbol{m}}_{\boldsymbol{2}}\big)\Big), \tag{A.17}$$

where $\mu_0 = 4\pi\cdot 10^{-7}[N\,A^{-2}]$ is the permeability of free space, $\mu_r[1]$ the characteristic relative permeability of the volume domain where the dipole-dipole interaction takes place (mostly the pumped fluid, which is water), $\boldsymbol{m_1} = \big(0,0,m_{1,z}\big)[A\,m^2]$ is the permanent magnet magnetic moment, $\boldsymbol{m_2} = \left(0,0,\underbrace{Nl_cI\pi r_{ow}^2}_{m_{2,z}}\right)[A\,m^2]$ the respective magnetic moment of a solenoid coil, for which $N[winding\ \ m^{-1}]$ is the wire coiling density or the number of windings per unit length assuming all are a single layer winding, $I[A]$ is the current running through the coil, and $l_c[m]$ the length of a single solenoid coil; last we define $\tilde{\boldsymbol{c}} = (C\lambda, 0, \tilde{z}(t))$ as the distance radius between the magnetic moment centers.

In calculating the distance between the centers of magnetic moment, we need to isolate our position in time within a duty cycle of solenoid train actuation. To do so, we correlate between the time and distance during a cycle,

$$\tilde{z}(t) = \underbrace{u_m\tau_r}_{z_0}(1-\not{f}), \tag{A.18}$$

whereby the nature of our actuation cycle: the magnet begins at $\tilde{z}(t) = z_0$, we then turn "on" the forward-positioned solenoid; the magnet travels at an approximated average velocity of $u_m = z_0/\tau_r$ until it reaches the activated solenoid magnetic moment center; we turn the solenoid "off", and the cycle repeats with the next forward-positioned solenoid. This sequence reliably describes a sawtooth wave function,

$$\not{f}(t) = \frac{A}{2} - \frac{A}{\pi} Arctan\left(Cot\left(\frac{\pi\, t}{\tau_r}\right)\right) \tag{A.19}$$

Where τ_r is a single solenoid relay period, and $A[1]$ is the coordinate strain for the temporal position $\not{f}$, meaning it strains the time coordinate such that at $t = 0$ the magnet center is a distance of z_0 from the forward-positioned solenoid, and when $t = \tau_r$ its position is $(1 - A) \cdot z_0$. Fig. S7 shows the magnet position during a duty cycle relative to forward activated ("on") solenoid as a function of time.

Last, we reason the introduction of the coordinate strain $A[1]$. Our simplified model (A.17) possesses a singularity, whereby at $|\tilde{\boldsymbol{c}}| = 0$, as the magnet and solenoid coil magnetic moments coincide spatially, the Maxwell force scalar $3\mu_0\mu_r|\boldsymbol{m_1}||\boldsymbol{m_2}|/4\pi|\tilde{\boldsymbol{c}}|^4$ goes to infinity. Correcting for this, we introduce the abovementioned coordinate strain $A[1]$, such that the magnetic core ending its travel periodically every $t = \tau_r$ maintains a fictitiously finite distance. We then evaluate this distance to produce the actual measured maximum Maxwell force. For details of this evaluation process, see section A.5.1.

Last, in using a point-like dipole-dipole interaction force, it is essential to address the two hidden assumptions held within and address their implication: first, we assume magnetic moment centers' distance radius is much greater than the characteristic length of the magnet $\tilde{z}(t) \gg l$; this model is otherwise only accurate for any distance and any finite magnet size when both dipoles are spherical magnets. Second, it is assumed that the poles in question cannot occupy the same space, hence the singularity at $\tilde{z} = 0$, where the Maxwell force scalar $3\mu_0\mu_r|\boldsymbol{m_1}||\boldsymbol{m_2}|/4\pi|\tilde{\boldsymbol{c}}|^4$ goes to infinity. As we do not strictly uphold either assumption; we propose a correction coefficient in the form of a coordinate strain $A[1]$, such that the magnetic core, ending its travel periodically every $t = \tau_r$, maintains a fictitious finite distance. We thus accommodate for a realistic maximum force cutoff when the magnet and solenoid magnetic centers coincide. For details of this evaluation process, see A.5.1.

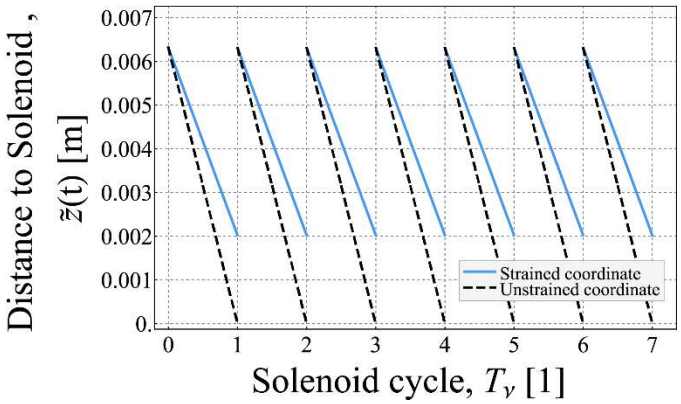

FIG. S7. ***Plot Showing the z-axis distance between magnetic moment centers' of permanent magnet and solenoid as a function of time during solenoid actuation sequence.*** *The figure follows the magnetic piston center of mass traveling at an approximated constant velocity* u_m*, taking* $\mathrm{t} = \tau_r[sec]$ *to travel from one solenoid to the next. The target-solenoid is then disengaged, and the next forward-positioned solenoid is turned on, and the cycle repeats; the sawtooth wave function* $\tilde{z}(t) = z_0\left(1 - A/2 + (A/\pi)Arctan\left(Cot(\pi\, t/\tau_r)\right)\right)$ *reliably describes this cycle. In dashed black, we present a non-strained temporal coordinate* $\mathrm{A} = 1[1]$*, and in pale blue, coordinate strain for the experimental system used in this study,* $A = 0.6797[1]$*. Plotted lines all use the following system parameters* $u_m = 0.334[m/sec]$*,* $z_0 = 0.006315[m]$ *and resulting relay period* $\tau_r = 0.0188 \pm 0.0007[sec]$ *taken as* $t_r \approx 0.019\ [sec]$*.*

Following, we calculate the magnetic dipole-dipole force expression for the force balance equations. Substituting the above-defined magnetic moments $\boldsymbol{m_1}$ and $\boldsymbol{m_2}$, the distance radius $\tilde{\boldsymbol{c}} = (C\lambda, 0, \tilde{z}(t))$, and scaling arguments into (A.17), we obtain the force expression in dimensional form,

$$\underbrace{\boldsymbol{f}_{b,2\to1}}_{\substack{Force\ by\ the\ magnetic\\ field\ of\ \ 2\ \ acting\ on\ 1}} = -\underbrace{\frac{3\mu_0\mu_r m_{1,z} N l_c I \pi r_{ow}^2}{4\pi\left(\sqrt{C^2\lambda^2+\tilde{z}(t)^2}\right)^4}}_{Force\ scalar\ magnitude}\left(\underbrace{\frac{C^3\lambda^3 - 4C\lambda\,\tilde{z}(t)^2}{\left(\sqrt{C^2\lambda^2+\tilde{z}(t)^2}\right)^3}}_{\hat{r}}, \underbrace{0}_{\hat{\theta}}, \underbrace{\frac{3\,\tilde{z}(t)C^2\lambda^2 - 2\tilde{z}(t)^3}{\left(\sqrt{C^2\lambda^2+\tilde{z}(t)^2}\right)^3}}_{\hat{z}}\right), \tag{A.20}$$

Preforming order separation based on our small parameter $\epsilon = C/L$, we obtain the leading order force term,

$O(1)$:

$$\underbrace{\boldsymbol{f}^{(0)}_{b,2\to1}}_{\substack{Force\ by\ the\ magnetic\\ field\ of\ \ 2\ \ acting\ on\ 1}} = -\underbrace{\frac{3\mu_0\mu_r m_{1,z} N l_c I \pi r_{ow}^2}{4\pi\left(\tilde{z}(t)\right)^4}}_{Force\ scalar\ magnitude}\left(\underbrace{0}_{\hat{r}}, \underbrace{0}_{\hat{\theta}}, \underbrace{-2}_{\hat{z}}\right), \tag{A.21}$$

and the first-order correction,

$O(\epsilon)$:

$$\underbrace{\boldsymbol{f}_{b,2\to1}^{(\epsilon)}}_{\substack{Force\ by\ the\ magnetic\\ field\ of\ \ 2\ \ acting\ on\ 1}} = -\frac{3\mu_0\mu_r m_{1,z} N l_c I\pi r_{ow}^2}{4\pi\left(\tilde{z}(t)\right)^4}\left(-\underbrace{\frac{4\lambda C}{\tilde{z}(t)}}_{\hat{\tilde{r}}}, \underbrace{0}_{\hat{\theta}}, \underbrace{0}_{\hat{z}}\right). \tag{A.22}$$

An important insight from this order correction is to elucidate the negligibility of the Maxwell force in our system as a centering force.

A.4.3. Explicit Solution - Singular Perturbation Asymptotic Expansion.

We now analyze system dynamics during the transient phase of the magnetic core prior to settling at an eccentric equilibrium position. The force balance equation (1.4) (see main text, section 4.1) shows the importance of controlling this transition phase. Our model predicts that the spatial velocity gradient $\partial u_z^{(0)}/\partial\tilde{r}$, governing the viscous friction term $\int_0^{2\pi}\int_{-l/2}^{l/2}\mu\left(\partial u_z^{(0)}/\partial\tilde{r}\right)\big|_{\tilde{r}=0} dz\, l\epsilon d\theta$, varies nonlinearly with eccentricity $\lambda(t)$ and its temporal gradient.

Seeking a perturbation solution to the non-dimensional leading order force balance in the $\tilde{r}$-axis detailing the transient magnet position during pumping operation (1.8). In attempting traditional singular perturbation approaches such as *Boundary-Layer Theory* or the *Method of Multiple Scales*, we encounter significant problems with order separation. In solving this, we propose a generalizable principle of reformulation and the introduction of a nonlinear evolution small parameter $\delta \in [0,1]$. We thus gradually evolve the nonlinearity incrementally until we reach the original form at $\delta = 1$. Reformulating equation (1.8) using this principle we obtain,

$$\underbrace{\left(\frac{t^*}{t_v^*}\right)\frac{(2\lambda^2\delta+1)}{(1+\lambda)(1-\lambda\delta)}\cdot\frac{1}{\left((1+\lambda)(1-\lambda\delta)\right)^{\frac{3}{2}\delta}}\frac{\partial\lambda}{\partial T_v}}_{\substack{axial\ viscous\ pressure\ lift\\ force}} + \underbrace{\lambda}_{\substack{ferrofluid\\ elastic\\ force}} - \underbrace{\varrho}_{\substack{External\ system\\ acceleration\\ force}} + \underbrace{\psi}_{\substack{Center-of\\ -pressure\\ force}} = 0\,, \tag{A.23}$$

with resulting characteristic scales for the viscous-elastic time scale $t^*{\sim}\pi l\mu/\epsilon^2\kappa_f$, the kinematic time scale $t_v^*{\sim}l/u_m$, and two non-dimensional numbers $\varrho = (radial\ accleration)/(Elastic\ forces) = ma_{\tilde{r}}/\kappa_f C$ and $\psi = (Destabilizing\ pressure)/(Elastic\ forces) = \gamma\mu u_m/\kappa_f$. The constants μ and

κ_f represent the ferrofluid's effective dynamic viscosity and linear spring coefficient, and γ the center-of-pressure coefficient relating back-pressure to the destabilizing force per unit length exerted on the levitated magnetic piston, which acts as an inverted pendulum.

Next, we address the reduction of the exponent δ in the first term, preventing order separation. We propose a first-order Taylor series approximation,

$$T_1^{\delta_0=0}\left(\left((1+\lambda)(1-\lambda\delta)\right)^{\frac{3}{2}\delta}\right)=\sum_{n=0}^{\infty}a_n\delta^n=1+\frac{3}{2}\ln(\lambda+1)\,\delta+O(\delta^2)\,, \tag{A.24}$$

and introduce a perturbation series of powers of δ for our eccentricity solution $\lambda(T_v)$,

$$\lambda(T_v,\delta)=\sum_{n=0}^{\infty}\lambda_n(T_v)\cdot\delta=\lambda_0(T_v)+\lambda_1(T_v)\delta+O\left(\delta^2\right). \tag{A.25}$$

Substituting (A.24) and (A.25) into (A.23) we are now able to obtain order separation; neglecting order higher then δ^1 it now reads,

$$\begin{aligned}\delta\Big(&-\lambda_0^3+\rho\lambda_0^2-\psi\lambda_0^2+\frac{3}{2}ln(\lambda_0+1)\,\lambda_0^2+2\frac{t^*}{t_v^*}\frac{\partial\lambda_0}{\partial T_v}\lambda_0^2-\lambda_0^2+\rho\lambda_0-\psi\lambda_0\\&-\frac{3}{2}\rho\,ln(\lambda_0+1)\,\lambda_0+\frac{3}{2}\psi\,ln(\lambda_0+1)\,\lambda_0+\frac{3}{2}ln(\lambda_0+1)\,\lambda_0\\&+2\lambda_1\lambda_0-\frac{3}{2}\rho\,ln(\lambda_0+1)+\frac{3}{2}\psi\,ln(\lambda_0+1)-\rho\lambda_1+\psi\lambda_1+\lambda_1\\&+\frac{t^*}{t_v^*}\frac{\partial\lambda_1}{\partial T_v}\Big)+\Lambda_0^2-\rho+\psi-\rho\lambda_0+\psi\lambda_0+\lambda_0+\frac{t^*}{t_v^*}\frac{\partial\lambda_0}{\partial T_v}=0\,.\end{aligned} \tag{A.26}$$

Separating for orders, we write the coefficient equations, with their respective IC,

$$O(\delta^0):\ \frac{t^*}{t_v^*}\frac{1}{(1+\Lambda_0)}\frac{\partial\lambda_0}{\partial T_v}+\lambda_0-\rho+\psi=0, \tag{A.27}$$

$$where\ \lambda_0(0)=0. \tag{A.28}$$

and,

$$\begin{aligned}O(\delta^1):\ &\frac{t^*}{t_v^*}\frac{\partial\lambda_1}{\partial T_v}+\lambda_1(2\lambda_0-\rho+\psi+1)\\&+\underbrace{\begin{pmatrix}-\lambda_0^3+\rho\lambda_0^2-\psi\lambda_0^2+\frac{3}{2}ln(\lambda_0+1)\,\lambda_0^2+2\frac{t^*}{t_v^*}\lambda_{0,T_v}\lambda_0^2\\-\lambda_0^2+\rho\lambda_0-\psi\lambda_0-\frac{3}{2}\rho\,ln(\lambda_0+1)\,\lambda_0\\+\frac{3}{2}\psi\,ln(\lambda_0+1)\,\lambda_0+\frac{3}{2}ln(\lambda_0+1)\,\lambda_0\\-\frac{3}{2}\rho\,ln(\lambda_0+1)+\frac{3}{2}\psi\,ln(\lambda_0+1)\end{pmatrix}}_{Heterogeneous\ term}=0,\end{aligned} \tag{A.29}$$

$$where\ \lambda_1(0)=0. \tag{A.30}$$

The resulting order separation produces in leading order equation, a non-linear ODE reducible to a canonic Bernoulli ODE, whose explicit solution is,

$$\lambda_0(T_\nu) = \frac{(\rho-\psi)\left(\mathrm{e}^{\rho T_\nu\left(\frac{t_\nu^*}{t^*}\right)+T_\nu\left(\frac{t_\nu^*}{t^*}\right)} - \mathrm{e}^{T_\nu\psi\left(\frac{t_\nu^*}{t^*}\right)}\right)}{\rho\mathrm{e}^{T_\nu\psi\left(\frac{t_\nu^*}{t^*}\right)} + \mathrm{e}^{\rho T_\nu\left(\frac{t_\nu^*}{t^*}\right)+T_\nu\left(\frac{t_\nu^*}{t^*}\right)} - \psi\mathrm{e}^{T_\nu\psi\left(\frac{t_\nu^*}{t^*}\right)}}. \tag{A.31}$$

The respective first-order correction (A.29) is a linear, first-order, heterogeneous ODE whose explicit solution is readily available. In Fig. S8, we present a comparison between leading (panel a) and first-order (panel b) approximation for $\delta = 0.5$, along with respective numerical solutions (dashed black) of the exact expression (1.8) (see main text, section 4.1); First-order approximation shows evident improvement in convergence to the numerical solution of the exact expression (dashed black), see Fig. S8b. It is noteworthy to point out that while it is of interest to investigate the convergence rate of the proposed method for higher orders and over a span of the nonlinear evolution parameter δ; within the scope of this paper, we suffice in using the leading-order approximation, $\delta = 0$, as the minimal and satisfactory expression to capture the transient governing physics from which both our goal of an explicit pump performance curve expression and insights can be obtained.

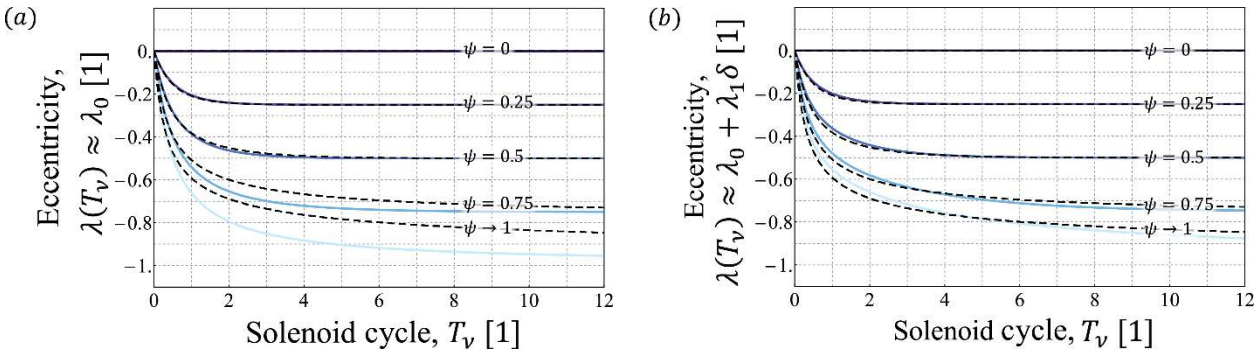

Fig. S8. ***Comparison of the approximate explicit solutions for leading and first-order corrections, confirming convergence to the respective numerical solution of the exact force balance expression in the $\tilde{r}$-axis, equation (1.8), see main text, section 4.1.*** *The time evolution of magnet position from an initial concentric position (at $\lambda = 0$) for different values of $\psi = \gamma\mu u_m/\kappa_f = \gamma\mu z_0/\kappa_f\tau_r$, by varying the relay time period τ_r. Presented is a quantitive comparison between the numerical solution (dashed black) of the exact expression* (A.23) *for $\delta = 1$ (original force blaalnce equation) and its explicit leading-order asymptotic approximation (A.31) in solid lines. (a) Leading order solution. (b) First-order solution. Color gradient of solid lines indicate respective values of $\psi =$* $[0, 0.25, 0.5, 0.75, 0.95]$.

A.4.4. Pump Performance Curve.

In this section, we present the step-by-step development of the pump performance curve from the z-axis force balance equation detail the dynamic balance of Maxwell stress terms, as are the result of dipole-dipole interaction between magnet and solenoid, with those from viscosity, gravity, and the rheology, with the latter resulting from the ferrofluid held by the magnetic field of the permanent magnet,

$$\hat{\boldsymbol{z}}\text{:}\ \underbrace{f_{b,2\to1,z}^{(0)}}_{\substack{Magnetic\ dipole\\ Maxwell\ force}} + \underbrace{\int_0^{2\pi}\int_{-l/2}^{l/2}\mu\left(\frac{\partial u_z^{(0)}}{\partial\tilde{r}}\right)\Big|_{\tilde{r}=0} dz\, l\epsilon d\theta}_{Circumferential\ friction\ pressure\ drop} - \underbrace{ma_z}_{\substack{External\ system\\ acceleration\\ force,\ z-axis}} - \underbrace{\pi(l\epsilon)^2\Delta p}_{\substack{Pressure\ drop\\ across\ piston}} = 0, \tag{A.32}$$

and present the full-form leading order slope curve $\Omega(q)$.

We begin by defining the duty cycle performance curve $\Delta p_{,DC}$ as the time-averaged pressure function,

$$\Delta p_{,DC} = \frac{1}{\tau_d}\int_0^{\tau_d}\Delta p(t)\,dt\,. \tag{A.33}$$

We set $\Delta p = p_{pump}$ and calculate our pump pressure or equivalently our equilibrium back-pressure as a function of time; substituting the explicit forms (1.6)(A.21), (1.3)(A.13) and reinstituting scaling arguments (A.3) into (1.4)(A.32), we obtain the explicit dimensional form of the z-axis force balance equation in terms of magnetic core velocity u_m, geometric and material parameters,

$$\underbrace{\frac{3\mu_0\mu_r m_{1,z}Nl_cI\pi r_{ow}^2}{2\pi\,\tilde{z}^4(t)}}_{\substack{Magnetic\ dipole\\ Maxwell\ force}} - \underbrace{\left(\underbrace{\pi(l\epsilon)^2\Delta p}_{\substack{hagen-poiseuille\\ flow}} + \underbrace{\frac{2\mu u_m\pi l}{\sqrt{1-\lambda^2(t)}}}_{Couette\ flow}\right)}_{Circumferential\ friction\ pressure\ drop} - \underbrace{ma_z}_{\substack{External\ system\\ acceleration\\ force,\ z-axis}} - \underbrace{\pi(l\epsilon)^2\Delta p}_{\substack{Pressure\ drop\\ across\ piston}} = 0. \tag{A.34}$$

Solving for $\Delta p(t)$ we obtain our systems performance curve in the form,

$$\Delta p(t) = \frac{\dfrac{3\mu_0\mu_r m_{1,z}Nl_cIr_{ow}^2}{2\,\tilde{z}^4(t)} - \dfrac{2\pi\mu u_m l}{\sqrt{1-\lambda^2(t)}} - ma_z}{2\pi C^2}. \tag{A.35}$$

Substituting $\lambda(t) \approx \lambda_0(t)$ with its explicit form (A.31) with $\varrho = 0$ (i.e. No external acceleration acting on the pump), and reinstituting scaling arguments we obtain the explicit form for magnet dynamics in our workbench setup. Substitute (A.18) and (A.19) into (A.35) we obtain the explicit form of $\Delta p(t)$,

$$\Delta p(t) = \left(\frac{3\mu_0\mu_r m_{1,z} N l_c I r_{ow}^2}{\pi z_0^4 \left(\frac{A\ arctan\left(\cot\left(\frac{\pi t}{\tau_r}\right)\right)}{\pi} - \frac{A}{2} + 1 \right)^4} - \frac{2a_z m}{\pi} - \frac{4l\mu u_m}{\sqrt{1 - \frac{\psi^2 (e^{t/t^*} - e^{t\psi/t^*})^2}{(e^{t/t^*} - \psi e^{t\psi/t^*})^2}}} \right) / 4C^2. \quad \text{(A.36)}$$

Substituting (A.36) into (A.33), then integrating over a single pumping duty cycle period τ_d and averaging, we obtain the pump performance curve $\Delta p_{,DC}$,

$$\begin{aligned} &\Delta p_{,DC} \\ &= -\frac{\mu l}{C^2} \underbrace{\Omega(q)}_{Curve\ slope} \\ &+ \underbrace{\frac{2\pi^2 \mu_0 \mu_r \tau_r m_{1,z} N l_c I r_{ow}^2}{A l^2 \tau_d z_0^4 \epsilon^2} \left(\frac{1}{\left(2A\ arctan\left(cot\left(\frac{\pi\tau_d}{\tau_r}\right)\right) - \pi(A-2)\right)^3} - \frac{1}{8\pi^3} \right)}_{Shut-off\ pressure,\ maximum\ pressure\ at\ q=0} - \underbrace{\frac{m a_z}{2\pi C^2}}_{\substack{Acceleration \\ component}}, \end{aligned} \quad \text{(A.37)}$$

where the slope function $\Omega(q)$ governing the form-function of the performance curve is,

$$\begin{aligned} &\Omega(q) \\ &= \frac{\mathrm{q}\, t^*}{\pi r_w^2} \left(\begin{array}{c} e^{-\frac{\tau_d}{t^*}} \left(e^{\frac{\tau_d}{t^*}} - \psi e^{\frac{\tau_d \psi}{t^*}} \right) \sqrt{\frac{2(\psi-1)\psi e^{\frac{\tau_d(\psi+1)}{t^*}} - (\psi^2-1) e^{\frac{2\tau_d}{t^*}}}{\left(e^{\frac{\tau_d}{t^*}} - \psi e^{\frac{\tau_d \psi}{t^*}} \right)^2}} \\ - \frac{2(\psi-1) e^{\frac{\tau_d(\psi+1)}{2t^*}} \sqrt{(\psi+1) e^{\frac{\tau_d - \tau_d\psi}{t^*}} - 2\psi}\ tanh^{-1}\left(\frac{\sqrt{\psi+1}\, e^{-\frac{\tau_d(\psi-1)}{2t^*}}}{\sqrt{(\psi+1) e^{\frac{\tau_d - \tau_d\psi}{t^*}} - 2\psi}} \right)}{\sqrt{\psi+1} \left(\psi e^{\frac{\tau_d\psi}{t^*}} - e^{\frac{\tau_d}{t^*}} \right) \sqrt{\frac{2(\psi-1)\psi e^{\frac{\tau_d(\psi+1)}{t^*}} - (\psi^2-1) e^{\frac{2\tau_d}{t^*}}}{\left(e^{\frac{\tau_d}{t^*}} - \psi e^{\frac{\tau_d \psi}{t^*}} \right)^2}}} \\ + \psi + \frac{2\sqrt{1-\psi}\ tanh^{-1}\left(\frac{\sqrt{\psi+1}}{\sqrt{1-\psi}} \right)}{\sqrt{\psi+1}} - 1 \end{array} \right) \\ &= \frac{}{-\tau_d(\psi-1)^2}. \end{aligned} \quad \text{(A.38)}$$

It is of particular interest to examine the slope curve $\Omega(\mathrm{q})$ at its asymptotic limit when $t^*/t_v^* \ll 1$. At this limit the center-of-pressure force, which is proportional to magnet kinetics, dominates the magnetic cores eccentric position; this is the case for systems with fast-moving magnetic pistons and low ferrofluid viscosity. Our magnet dynamic's governing equation (A.23) becomes algebraic,

$$\underbrace{\lambda}_{\substack{ferrofluid \\ elastic \\ force}} - \underbrace{\varrho}_{\substack{External\ system \\ acceleration \\ force}} + \underbrace{\psi}_{\substack{Center-of \\ -pressure \\ force}} = 0\,. \quad \text{(A.39)}$$

Reinstituting scaling arguments, and solving for λ,

$$\lambda = -\underbrace{\frac{\gamma\mu}{\kappa_f}u_m}_{\substack{Center-of\\-pressure\\force}} + \underbrace{\frac{ma_{\tilde{r}}}{\kappa_f C}}_{\substack{System\\acceleration\\force}} \quad , \quad \left(\frac{t^*}{t_v^*}\right) \ll 1. \tag{A.40}$$

We repeat the process detailed in equations (A.33) - (A.37); this time substituting (A.40) instead of (A.31), we obtain the asymptotic limit for $\Omega(\mathrm{q})$ when $t^*/t_v^* \ll 1$,

$$\Omega(\mathrm{q}) \sim q/\pi \mathrm{r}_\mathrm{w}^2 \sqrt{1 - \left(\underbrace{(a_{\tilde{r}} m \pi \mathrm{r}_\mathrm{w}^2 - \gamma C \mu q)/C\kappa_f \pi \mathrm{r}_\mathrm{w}^2}_{=\lambda_{ss}}\right)^2}, \tag{A.41}$$

where λ_{ss} is the steady-state eccentric position of the magnetic piston. This simplified limit-form informs qualitative insights into parameters relations' to curve steepness.

A.5. Characterization of System Parameters.

A.5.1. Estimation of Coordinate Strain Parameter A.

To calculate the coordinate strain coefficient, we extract the strain parameter $A[1]$ from the shut-off pressure by substituting $\Delta p_{,DC} = p_{shut-off}$ and $q = 0$ into (A.37) (equation (1.11) from the main text, see section 4.1) resulting in,

$$p_{\substack{shut\\-off}} = \underbrace{\frac{2\pi^2 \mu_0 \mu_r \tau_r m_{1,z} N l_c I r_{ow}^2}{A l^2 \tau_d z_0^4 \epsilon^2}\left(\frac{1}{\left(2A\, arctan\left(cot\left(\frac{\pi\tau_d}{\tau_r}\right)\right) - \pi(A-2)\right)^3} - \frac{1}{8\pi^3}\right)}_{Shut-off\ pressure,\ maximum\ pressure\ at\ q=0} - \underbrace{\frac{ma_z}{2\pi C^2}}_{\substack{Acceleration\\component}}; \tag{A.42}$$

substituting the shut-off pressure (i.e., the trivially measured pressure when the outlet is plugged) we can solve for $A[1]$. Finally, substituting proposed experimental system parameters and solving, we obtain our ESP temporal strain coefficient $A = 0.6797[1]$.

A.5.2. Evaluation Minimal Solenoid Relay Time, τ_r.

In evaluating the minimal solenoid relay time experimentally, we propose two methods. First, having measured the max flow rate at run-out, $\mathrm{q_{max}} = 320 \pm 12\ [\mathrm{ml/min}] = (5.33 \pm 0.2) \cdot$

10^{-6} [m^3/sec] we can then calculate the minimal relay time using flow rate definition $q_{max} = \left(\underbrace{z_0/\tau_{r,min}}_{u_m}\right)\pi\left(\underbrace{r_m + C}_{\substack{Inner\ wall \\ radius}}\right)^2$; with $r_m = 0.002[m]$ and $z_0 = 6.315 \cdot 10^{-3}[m]$. Solving for $\tau_{r,min}$ we estimate $\tau_{r,min,exp} = 0.0188 \pm 0.0007\ [sec]$ taken as $t_{r,min,exp} \approx 0.019$[sec] for most calculations in the study. Second, we propose measuring the magnet travel time from the center of one solenoid to the next using ultrasound scanning. The ultrasound transducer (Philips, L18-5) and the ESP were positioned in the ultrasound transducer holder, as shown in Fig. S9a and S9b. Holder maintained the constant distance between the ESP and the ultrasound transducer. In order to conduct the ultrasound scanning experiment, we constructed a copper solenoid with a 1 $[mm]$ gap at the center as ultrasound cannot pass through the copper wiring (Fig. S9c and S9d). Therefore, the location of the magnet can be detected. In order to produce an identical magnetic field, the updated coil (i.e., with a one-millimeter gap at its center) had its number of windings updated so that its radius, coil density, copper wire diameter, and applied current all remained constant. Figure S9e shows the ultrasound images used to analyze the movement of the magnet. Ultrasound images are captured every 5[ms]; estimating a nominal relay time of $\tau_{r,nom,exp} = 0.020 \pm 0.005$[sec]. The ultrasound and flow rate-based relay time, agree within 6% nominally.

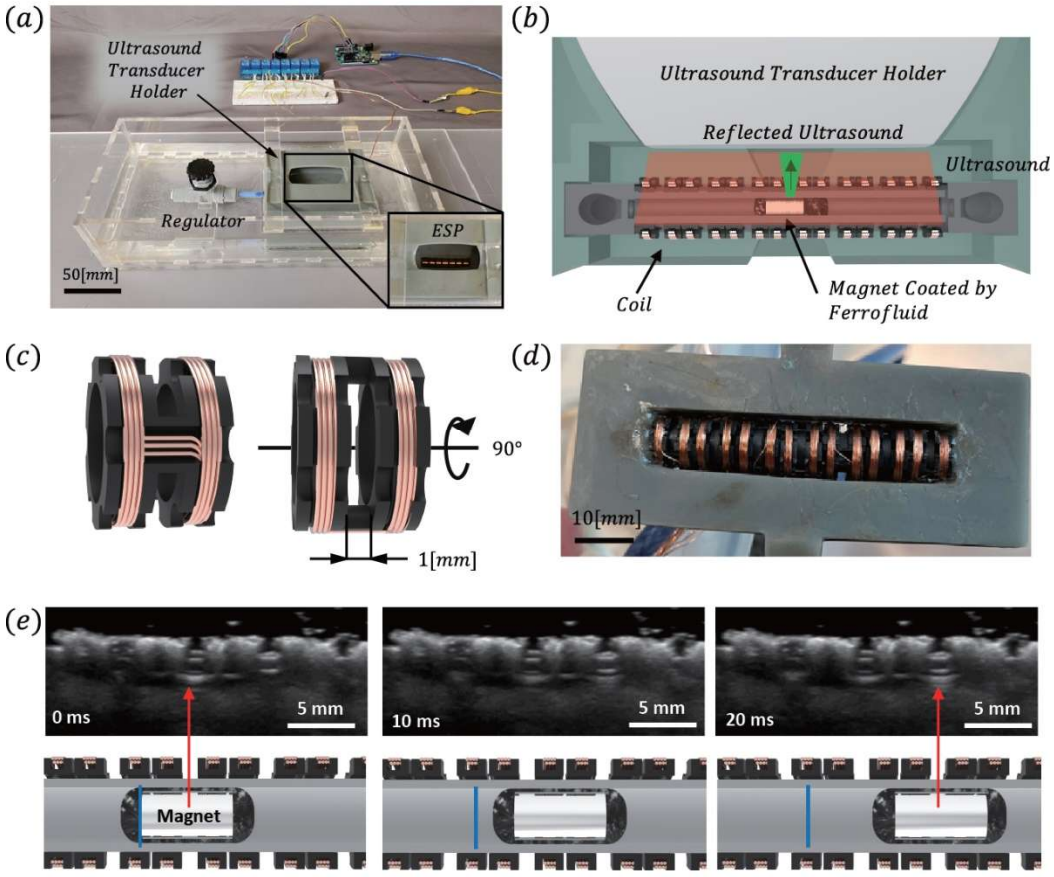

Fig. S9. ***Ultrasound scanning for measuring magnet minimal relay time.*** *(a) Photo of the ultrasound scanning setup. (b) Schematic illustration of the ultrasound scanning setup. (c) Schematic illustration of the updated coil with the* $1\ [mm]$ *gap at its center (d) Image of the assembled ESP used for ultrasound scanning experiment. (e) Ultrasound scanned images and corresponding schematic illustrations at* 0*,* 10*, and* $20\ [ms]$ *after activating the forward driving solenoid.*

A.5.3. Estimation of Ferrofluid Linear Spring Coefficient κ_f.

Magnetically saturated ferrofluids exhibit the ability to form and hold their shape by an induced distributed magnetic volume force. To capture this effect in $\tilde{r}$-axis force balance, see main text section 4.1 equation (1.5), we seek a simplified and sufficient model. We propose a simple linear spring model,

$$f_{\substack{mag, \\ ferro}} = \kappa_f \cdot \Delta r\ , \tag{A.43}$$

Where $\Delta r[m]$ is the radial strain applied to the ferrofluid droplet, and $\kappa_f[N/m]$ the effective linear spring coefficient. To measure this effective spring coefficient, we mount an identical magnet as is used in the experimental setup; to ensure we induce an equivalent distributed magnetic volume force in the ferrofluid. We then apply FerroTec EFH1 ferrofluid to the magnet, forming a node at each pole end. The nodes in this setup collect at the magnetic poles rather than coat the magnet as they are unrestrained,

as would be the case inside the ESP core tube; however, it is inconsequential in measuring the spring coefficient. Using a scale (Mettler Toledo), we measure the weight increase as the micrometer probe end strains the ferrofluid coat (the end attachment is made of aluminum to avoid magnetic interference). Fig. S10(a-c) shows the experimental setup, Fig, S10d presents experimental data; the curve informs parameter κ_f as the force measured corresponds to the effective linear spring coefficient. The effective linear spring coefficient calculated for Ferrotec EFH1 in this setup is $\kappa_f = 0.667[N/m]$; error indicates a 68% confidence (one standard deviation) in the mean based on seven separate experiments.

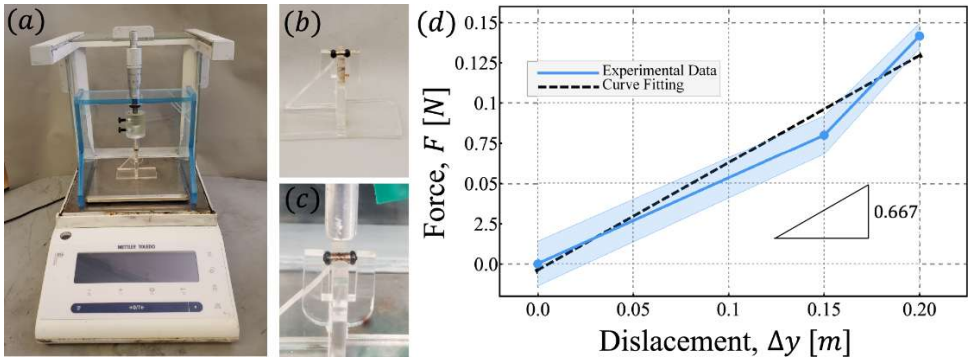

Fig. S10. ***Experimental setup for ferrofluid linear spring coefficient κ_f measurement.*** *(a) experimental setup; micrometer (Mitutoyo), with the AL end attachment used to strain the ferrofluid nodes. Each node is approximately* $0.5\ [mm]$ *thick. (b) closeup of the magnet mounting jig. (c) closeup of probe prior to contact with mounted magnet during an experiment. (d) Experimental measurement of linear spring coefficient* κ_f*. Error bands indicate a 68% confidence (one standard deviation) in the mean based on seven experiments; markers represent the experimental mean value.*

A.5.4. Evaluation of Center-of-pressure Coefficient, γ.

In Calculating the center-of-pressure coefficient $\gamma[1]$, we substitute $\Delta p_{,DC} = \Delta p = 0,\ q = q_{max}$ into the pump performance curve $\Delta p_{,DC}$, equation (A.37) (main text section 4.1, equation (1.11)) and solve for γ. Fig. S11 we present the numerical solution locating zeros, by which we find $\gamma = 2255[1]$.

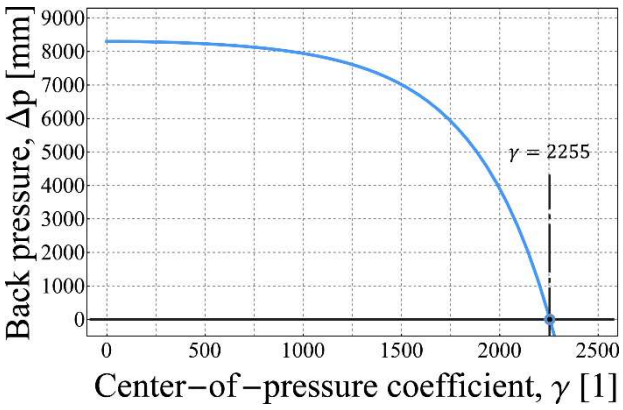

Fig. S11. ***Theoretical evaluation of center-of-pressure coefficient γ.*** *Numerical solution for equation (A.37) solving for γ when $\Delta p_{,DC} = \Delta p = 0$ and $q = q_{max}$. The curve informs parameter γ, evaluated at $\gamma = 2255[1]$.*

A.6. Numerical Investigation of Viscous Fingering Phenomena.

Examining the pump performance, we turn to investigate how a constant velocity-driven positive displacement pump, whereby magnet velocity $u_{mag} = z_0/\tau_r$ is held constant, provides a varying flow rate q. Utilizing the equation-based modeling capabilities of COMSOL Multiphysics 5.5, we investigate the 2D flow within the Hele-Shaw cell with a variable height. We map our gap curvilinear coordinate system $(\tilde{r}, \theta, z)$ onto a 2D cartesian plane $z - y$, and model the variable Hele-Shaw cell height by the gap curvilinear coordinate in the $\tilde{r}$-axis,

$$h(\theta = y/r_m) = r_w - r_m = \begin{matrix} Gap\ measure\ in \\ gap\ curvlinear\ coordinate \end{matrix} = r_m\epsilon\lambda\cos(y/r_m) + \sqrt{\left(r_m(1+\epsilon)\right)^2 - (r_m\epsilon\lambda)^2 + (r_m\epsilon\lambda\cos(y/r_m))^2} - r_m\ ; \quad \text{(A.44)}$$

for more details on the gap curvilinear coordinate system, see section A.4. The fluid domain consists of two immiscible Newtonian fluids: the pumped fluid (pale blue), water with dynamic viscosity $\mu_1 = 0.0008[Pa \cdot sec]$, and ferrofluid (dark gray) seal, with dynamic viscosity $\mu_1 = 0.006[Pa \cdot sec]$. The Hele-Shaw cell plane is of width $y_{dim} = 2\pi r_m$ and length $z_{dim} = l + \delta l$ where $r_m[m]$ is magnet radius, $l[m]$ is permanent magnet length and $\delta l = 0.001[m]$ an arbitrary small added length in the flow direction for visual clarity such that the ferrofluid seal front starts away from the fluid domain boundary.

Previous work [76–78] aimed at investigating the emergence of the Saffman-Taylor instability in constant cross-section Hele-Shaw cells in the presence of pressure-driven flow of displacing low dynamic viscosity fluid (μ_1, water) forcing out a resident fluid of higher dynamic viscosity (μ_2, oil). We modify the model to address the unique physics prevalent in our system. First, the dipole-dipole interaction between ferrofluid and both permanent magnet and forward driving solenoid. Second, solving for a Hele-Shaw cell with a spatially non-uniform gap geometry.

We begin by formulating the conservation of mass for incompressible flow $\nabla \cdot \boldsymbol{u} = 0$ with $\boldsymbol{u} = (u_z, u_y)$ a two-dimensional velocity vector in the z and y axis respectively and the del operator $\nabla = (\partial/\partial z, \partial/\partial y)$. We apply conservation of momentum in the form of a modified Darcy's law for porous media flow $\boldsymbol{u} = -\frac{\boldsymbol{k}}{\mu}\nabla p + \boldsymbol{\Pi_b^{(0)}}$, where the permeability tensor is simplified to a gap dependent scalar $\boldsymbol{k} = k = h^2(y)\,/12[m^2]$, the dynamic viscosity $\mu = \mu(c_f)$ is a function of the solute concentration variable by which we differentiate between the fluids (further discussed below), p is the fluid pressure, and $\boldsymbol{\Pi_b^{(0)}} = \boldsymbol{\Pi_{b,1\to3}^{(0)}} + \boldsymbol{\Pi_{b,2\to3}^{(0)}}$ is the adverse Maxwell pressure vector due to magnet-ferrofluid and solenoid-ferrofluid dipole-dipole interaction averaged over a characteristic length,

$$\underbrace{\boldsymbol{\Pi_{b,1\to3}^{(0)}}}_{\substack{Maxwell\ force,\\ Magnet\to Ferrofluid}} = \begin{pmatrix} \int_0^z \frac{\boldsymbol{k}}{\mu}\frac{c_f(z,y)}{l^2}\sin(4\pi z/l)\,dz \underbrace{\frac{\left(\frac{3\mu_0\mu_r m_{1,z}m_{3,z}}{2\pi\left(\sqrt{r_m^2+(l/2)^2}\right)^4}\right)}{\int_0^{2\pi} h(\theta)r_m\,d\theta}}_{Maxwell\ pressure}, \\ \int_0^y \frac{\boldsymbol{k}}{\mu}\frac{c_f(z,y)}{(2\pi r_m)^2}\sin(y/r_m)\,dy \underbrace{\frac{\left(\frac{3\mu_0\mu_r m_{1,y}m_{3,y}}{2\pi\left(\sqrt{r_m^2+(l/2)^2}\right)^4}\right)}{\int_0^{2\pi} h(\theta)r_m\,d\theta}}_{Maxwell\ pressure} \end{pmatrix}, \tag{A.45}$$

$$\underbrace{\boldsymbol{\Pi_{b,2\to3}^{(0)}}}_{\substack{Maxwell\ force,\\ Solenoid\to Ferrofluid}} = \begin{pmatrix} -\int_0^z \frac{\boldsymbol{k}}{\mu}\frac{c_f(z,y)}{l^2}dz \underbrace{\frac{\left(\frac{3\mu_0\mu_r m_{2,z}m_{3,z}}{2\pi\left(\tilde{z}(t)\right)^4}\right)}{\int_0^{2\pi} h(\theta)r_m\,d\theta}}_{Maxwell\ pressure}, \\ \int_0^y \frac{\boldsymbol{k}}{\mu}\frac{c_f(z,y)}{(2\pi r_m)^2}dy \underbrace{\frac{\left(\frac{3\mu_0\mu_r m_{2,y}m_{3,y}}{2\pi\left(\tilde{z}(t)\right)^4}\right)}{\int_0^{2\pi} h(\theta)r_m\,d\theta}}_{Maxwell\ pressure} \end{pmatrix}. \tag{A.46}$$

Where $\boldsymbol{m_1} = (0.015,0)[m^2\,A]$ is the permanent magnet magnetic moment, for which $|\boldsymbol{m_1}| = H_{ci,mag}[A/m]\cdot\mathcal{V}_{mag}[m^3]$, with $H_{ci,mag}$ the magnetic field strength of the magnet (i.e., magnetic

piston core), as detailed in the manufacturer datasheet, and $\mathcal{V}_{mag}$ the volume of the magnet; $\boldsymbol{m_2} = (4.85 \cdot 10^{-4}, 0)[m^2\ A]$ is the magnetic moment of a solenoid coil, $|\boldsymbol{m_2}| = N l_c I \pi r_{ow}^2$, for which $N[winding\ \ m^{-1}]$ is the wire coiling density or the number of windings per unit length assuming all are a single layer winding, $I[A]$ is the current running through the coil, and $l_c[m]$ the length of a single solenoid coil; last, $\boldsymbol{m_3} = (7.38 \cdot 10^{-4}, 0)[m^2\ A]$ is the magnetic dipole moment of the saturated ferrofluid, where $|\boldsymbol{m_3}| = H_{ci,ferro}[A/m] \cdot \mathcal{V}_{ferro}[m^3]$, with $H_{ci,ferro}$ the magnetic field strength of the saturated ferrofluid, as detailed in the manufacturer datasheet, and $\mathcal{V}_{ferro}$ the volume of the ferrofluid seal.

Using this simplistic model, we capture the underlying physical phenomena of these far more complex superimposed dipole-dipole interactions. These simplifications include: neglection of interfacial tension effects from the choice of particular fluids, neglection of circumferential dipole-dipole interactions, neglection of capillary action and surface tension, and last we averaging along characteristic dimensions. All these lend to a stable convergent model at the expense of quantitative accuracy; an acceptable compromise in the case of this study, as the sole aim of this model is to inform as to the unique emergence of stable oscillating viscous fingers patterns in the presence of restoring Maxwell forces under these conditions. We thus reason the means by which a constant velocity-driven positive displacement pump provides a varying flow rate q; as an effective steady-state flow rate "leak" is established and maintained past the ferrofluid seal.

In our model, we set viscosity as concentration-dependent $\mu = \mu(c_f)$; we conveniently follow Zimmerman and Homsey [77] and propose $(1/\mu)\partial\mu/\partial c_f = -\mathcal{R}$ such that $\mathcal{R} = \ln(M)$ where $M = \mu_1/\mu_2$ is the mobility ratio. This simplified model suggest viscosity decreases exponentially with solute concentration variable c_f, such that $c_f = 1$ is the viscosity of μ_1 (the less viscous - water) and $c_f = 0$, is the viscosity of μ_2 (higher viscosity - ferrofluid). Solving $\mu(c_f)$ we find the fluid viscosity fucntion $\mu = \mu(c_f) = \mu_2\, e^{-c_f \ln(M)}$.

Next, we formulate the solute transport of the fluid interface in the form of an advection-diffusion equation over the concentration-independent variable $c_f[1]$,

$$\phi \frac{\partial c_f}{\partial t} = \nabla \cdot (\boldsymbol{D}\nabla) c_f - \boldsymbol{u} \cdot \nabla c_f \, . \tag{A.47}$$

The dispersion tensor is given by

$$\boldsymbol{D} = \begin{pmatrix} \frac{\left(\alpha_L u_z^2 + \alpha_T u_y^2\right)}{||\boldsymbol{u}||} & \frac{(\alpha_L - \alpha_T) u_z u_y}{||\boldsymbol{u}||} \\ \frac{(\alpha_L - \alpha_T) u_z u_y}{||\boldsymbol{u}||} & \frac{\left(\alpha_L u_y^2 + \alpha_T u_z^2\right)}{||\boldsymbol{u}||} \end{pmatrix} \left[\frac{m^2}{sec}\right], \tag{A.48}$$

following in the steps of Coutinho and Alves [76]. We define: the local fluid velocity magnitude of $||\boldsymbol{u}|| = \sqrt{u_z^2 + u_y^2}$; the longitudinal dispersive length as $\alpha_L = \mathcal{D}_L(U)/U + \alpha_T \left(1 - (u_z/U)^2 - \left(u_y/U\right)^2\right)$, for which the longitudinal dispersion (often simply referred to as dispersion) is empirically defined according to [79,80] as $\mathcal{D}_L(u) = \mathcal{D}_0 + (2/105)(C^2 u^2/\mathcal{D}_0)$; the transversal dispersive length $\alpha_T = \mathcal{D}_0/U$ defined by the molecular diffusivity $\mathcal{D}_0 = 2.299 \cdot 10^{-9}[m^2/sec]$ (taken to be that of water at $25[℃]$). Last we define $U = u_{leak} = \frac{q_{max} - q}{\pi r_w^2}$ our superficial or characteristic velocity, which is the average leak velocity past the ferrofluid seal; as we infer from the difference between the known run-out flow rate $q_{max}[m^3/sec]$ and the resulting flow rate $q[m^3/sec]$ at the outlet.

Concluding our model, we set the boundary and initial conditions for a well-posed problem. Our system starts from rest setting $p(z, y, 0) = 0$, $(\partial p(z, y, t)/\partial t)|_{t=0} = 0$ over the fluid field; for the transport equation, we define the fluid-fluid interface $c_f(z, y, o) = \left(1 - H(z - z_i)\right) + \zeta f(z, y) \exp\left(-(z - z_i)^2/\sigma^2\right)$ in which $H(z - z_i)$ is a Heaviside step function positioned at $z_i = 0[m]$, providing the initial position of the fluid-fluid interface, $\zeta = z_{dim} \cdot 10^{-4}[m]$ denotes the size of the random disturbance initial pattern $f(x, y)$ and last, $\sigma = l[m]$ gives its variance in the z-direction. Finally, we define boundary conditions for the inlet velocity $(-(k/\mu)\, \partial p/\partial z)|_{z=0} = u_{leak}$, the ambient pressure at the outlet $p(l, y, t) = 0$, and symmetry conditions for the top and bottom walls such that: $p(z, 0, t) = p(z, 2\pi r_m, t)$ and $(\partial p(z, y, t)/\partial y)|_{y=0} = (\partial p(z, y, t)/\partial y)|_{y=2\pi r_m}$.

Figure S12 presents a system illustration examining the transient evolution of the ferrofluid seal front from both a 2D top view and 3D projection. Panel (a) shows system schematics, illustrating the 3D to 2D mapping and the 2D fluid domain solved for. Panel (b) - (d) show Snapshots of the system at optimal work point $q_{ss} \approx 225\ [ml\ min^{-1}]$ with respective parameters $\psi = 4.8$ and $|\lambda_{ss}| \to 1$, for time $t \approx 0.011,\ 0.022$ and $t \gg O(t^*)\ [sec]$ respectively. Column (I) shows the ferrofluid seal front evolution in a theoretical system absent of the Maxwell restoring forces; steady-state in this case will be at $t \to \infty$ as ferrofluid seal will exponentially decay until it is all washed away. Opposing it, in column (II), we show identical time snapshots; the system achieves a stable oscillating viscous finger pattern for $t > O(t^*)$ at solenoid-train actuation frequency, see Movie S3 and S4.

In conclusion, the qualitative effects of restoring Maxwell forces are evident. First is the reduction of the leak cross-section (the breach seen in pale blue past the boundary at $z = l$), leading to an increase in generated pump pressure. We provide experimental evidence for this conclusion in the main text, section A.4.4 figure 4c, where we compare performance *with* (black line) and *without* (red line) ferrofluid; respective to column *(II)* where the seal is maintained in steady-state, while column *(I)* where all ferrofluid is stripped (washed away) from the magnet in the absence of restoring Maxwell forces. Second, we demonstrate the emergence of the hypothesized stable oscillating viscous finger structure, maintained by the unique force equilibrium between Maxwell and viscous forces.

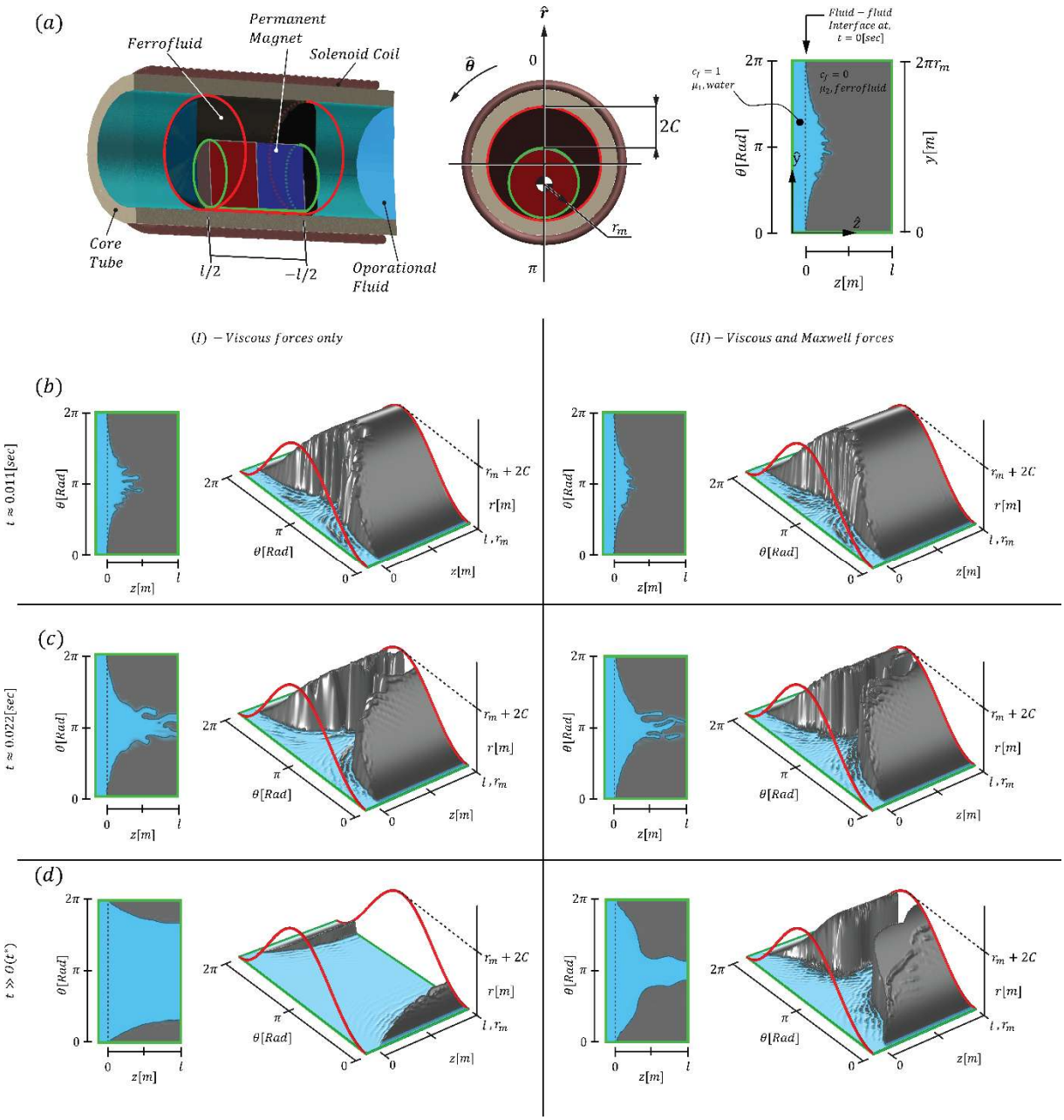

Fig. S12. ***Results of numerical simulations of ferrofluid seal dynamics in the presence and absence of Maxwell dipole-dipole interactions between magnet, solenoid, and ferrofluid.*** *Snapshots examine ferrofluid seal front evolution at optimal work point at* $q_{ss} \approx 225\ [ml\ min^{-1}]$ *with respective parameters* $\psi = 4.8$ *and* $|\lambda_{ss}| \to 1$. *We mark the ferrofluid in dark gray and pump fluid (water) pale blue. Column (I) shows the resulting seal front in the presence of viscous friction alone; Column (II) shows the resulting seal front due to viscous friction and the Maxwell forces from dipole-dipole interaction of ferrofluid with both magnet and solenoid coil. (a) Illustration of examined configuration and schematics of the flow system. We visualize the inner core tube diameter (red) and magnet outer diameter (green) to clarify the coordinate mapping in the subsequent panels. (b) The emergence of distinct viscous fingers (Saffman-Taylor instability) at* $\mathrm{t} \approx 0.011[sec]$. *(c) Snapshot of seal front at* $\mathrm{t} \approx 0.022[\mathrm{sec}]$, *viscous fingers complete growth prior to seal breach. (d) Snapshot of seal front at* $t \gg O(t^*)[sec]$, *seal front remaining has either achieved steady-state and will retain its form over time by force equilibrium, Column (II), or remaining ferrofluid seal will continue to exponentially decay until it is all washed away, Column (I).*

A.7. Strain Rate Estimation

We define the non-dimensional strain rate based on the experimental data Fig. 7c (see main text, section 5) as,

$$\dot{\mathrm{E}} = \frac{(\Delta\ell/\ell_0)}{\Delta t/t^*}, \tag{A.49}$$

where $t^* \sim \pi l\mu/\epsilon^2\kappa_f \approx 0.113[\mathrm{sec}]$ is the viscous elastic time scale.

Deformation	**Section**	$\boldsymbol{t_{init}[sec]}$	$\boldsymbol{t_{end}[sec]}$	$\boldsymbol{\Delta\ell/\ell_0}$ **[1]**	$\dot{\mathbf{E}}$ **[1]**
Contraction	(*II*)	1.6	3	0.15	0.012
Bend	(*III*)	5.1	5.7	20°/180°	0.020
Bend	(*IV*)	6.7	7.6	20°/180°	0.013

TABLE. A.2. ***Tabulated data and calculated non-dimensional strain rate $\dot{E}$ during obstruction course dynamic deformation***.